Master thesis in Physical Oceanography

- Climate dynamics

Rapid changes in the Subpolar Gyre based on an Ocean General Circulation Model

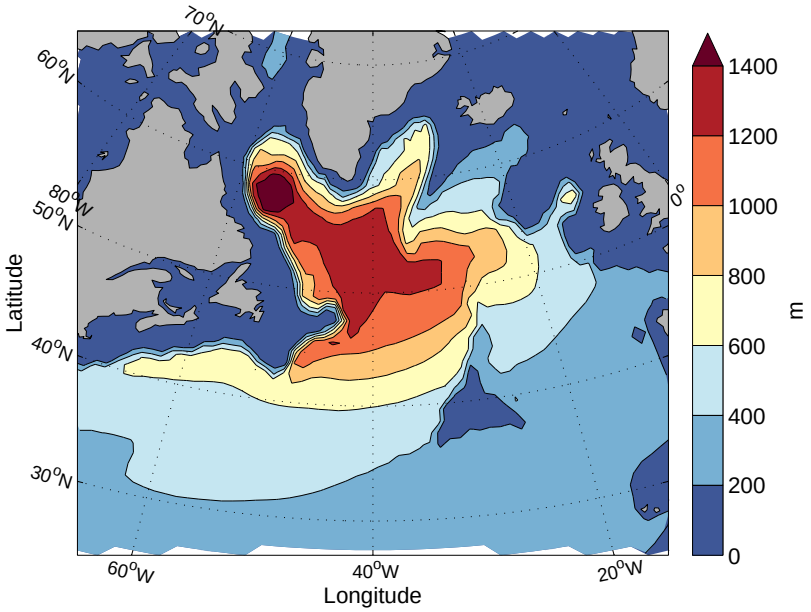

Torgeir Blesvik

3rd June 2013

UNIVERSITY OF BERGEN
GEOPHYSICAL INSTITUTE

The figure on the front page illustrates the mean layer thickness of model layer 33 in March for the ERA40 based NAO^+ composite.

Først og fremst vil eg retta ein stor takk til rettleiaren min Helge Drange, som har vore eksemplarisk, med positiv innstilling og verdfulle rettleiingar. Ein stor takk går også til Mats Bentsen og Ingo Bethke, for all hjelp med modelldata.

Abstract

Data from the ocean component of the Norwegian Earth System Model has been analyzed for the period 1960-2008. Most attention is given to the Subpolar Gyre, which strength and spatial extensiveness is understood to have major consequences for the marine climate in the North Atlantic. Variations in the ocean temperature and salinity are mainly found in the upper few hundred meters, to a large degree dictated by the atmospheric forcing. The Labrador Sea is the region which shows largest response to the atmospheric forcing, and is a major source for variations in the Atlantic Meridional Ocean Circulation at 41°N. In the Labrador Sea, the convective mixing during strong cooling events reaches down to 2000-2500 m and increases the thickness of the isopycnic layer of potential density 1036.843 kg m^{-3} (relative to 2000 m depth) by approximately 500 m relative to the climatological mean value. This water mass more than double in volume between a minimum in 1970 and a maximum in 1995. Using an idealised model and Margules relation, we have shown that a 5 Sverdrup (1 Sv $= 10^6$ m^3 s^{-1}) intensification of the barotropic streamfunction for strong versus normal years expressed in terms of the North Atlantic Oscillation (NAO) index is consistent with roughly an increase in the geostrophic flow of 15%. Using composites from a NAO index derived from two-station and spatial pattern-based sea level pressure differences show negligible to large differences in the upper ocean response to the atmospheric forcing, depending on the actual analyzes examined.

Contents

Chapter 1

Introduction

The North Atlantic Subpolar Gyre (SPG) is a major ocean circulation pattern of relative cold and low-saline subarctic water located in the central northern North Atlantic (Hatun et al., 2009). During winter, cold winds remove heat from the ocean at rates of several hundred watts per square meter, resulting in deep convection reaching as far as 2500 m below the surface (Häkkinen and Rhines, 2004). This deep water is an important contributor to the southward deep flow which is part of the Atlantic Meridional Ocean Circulation (AMOC) (Bentsen et al., 2004). The northward component of the AMOC compensate the southward deep flow, bringing warm and saline waters in the upper ocean towards the northern North Atlantic.

Observations since the instrumental measurments started about 100 years ago reveal large variations in the North Atlantic climate. Two major warming periods in the North Atlantic occured during the 1920s-1960s and 1990s-2000s (Drinkwater, 2009). The increase in ocean temperature led to northward migration of different fish-species (Drinkwater, 2006, 2009). High temperatures also influence the retreat rates of the ocean outlet glaciers towards the ocean, and is a likely contributor to the rapid melting of Greenland's glaciers observed during the 2000s (Holland et al., 2008). Large variations in the marine climate and ecosystems are linked with changes in the strength and extent of the SPG (Hatun et al., 2009). Thus, understanding the variations of the SPG is an important issue for the prediction and understanding of the North Atlantic climate.

The aim of this thesis is to provide an understanding of the basic mechanisms and

dynamics behind the variations in the SPG. The analyzes are based on model simulations of ocean climate from 1960-2008 supported by some observation data. Using an Ocean General Circulation Model (OGCM) as the major source for data is of course inferior to build the analysis on in situ observations. Unfortuneately, relatively few observations are available for the region and time interval considered here. The OGCM used in this study, and the earlier versions, has demonstrated skill in simulating the mean climate and interannual to decadal variations in the region of interest (Hatun et al., 2005; Lohmann et al., 2008, 2009; Bentsen et al., 2013).

The thesis is structured as follows; the theory and background behind the most central subjects concerned with the SPG, are presented in Chapter 2. Chapter 3 describes the numerical model. In Chapter 4, the results from the analyzes of the model and observations are presented. In Chapter 5, some of the central findings in the results will be discussed. The thesis will be concluded with a summary and outlook in Chapter 6. Statistical methods used in this study are decribed in Appendix.

Chapter 2

Theory

2.1 Oceanographic Setting

The SPG, shown in Fig. 2.1, is a cyclonic (anticlockwise) ocean circulation which is typically confined to the region between 50°N and 65°N in the North Atlantic (Häkkinen and Rhines, 2004). At south it extends to the North Atlantic Current (NAC) which is an extension of the Gulf Stream (Stein, 2005), mainly confined to the upper 700 m of the ocean (Talley et al., 2011, p. 282). NAC itself carries warm and saline water into the northern North Atlantic, contributing to the mild climate in northern and northwestern Europe (Seager et al., 2002). A northward branch of the NAC follows a route west of Iceland, known as the Irminger current (Talley et al., 2011, p. 262). This current turns west and south and continues along the northern boundary of the SPG, where it finally reaches the southward Labrador current.

South of the NAC, the anticyclonic subtropical gyre (STG) is located, extending to about 15°N. A weak SPG corresponds to a westward retreat of the cold and fresh subarctic front in the eastern SPG (Häkkinen and Rhines, 2009). This allows the STG to extend northeastward which advects warm and high-salinity waters towards the Nordic Seas and the Arctic Ocean in north, and towards west via the Irminger current. The location, intensity and composition of the NAC which is placed along the boundary between the two gyres are also affected (Hatun et al., 2005). As pointed out in Holland et al. (2008), this water will supply the coast of Greenland and western part of the SPG with relative

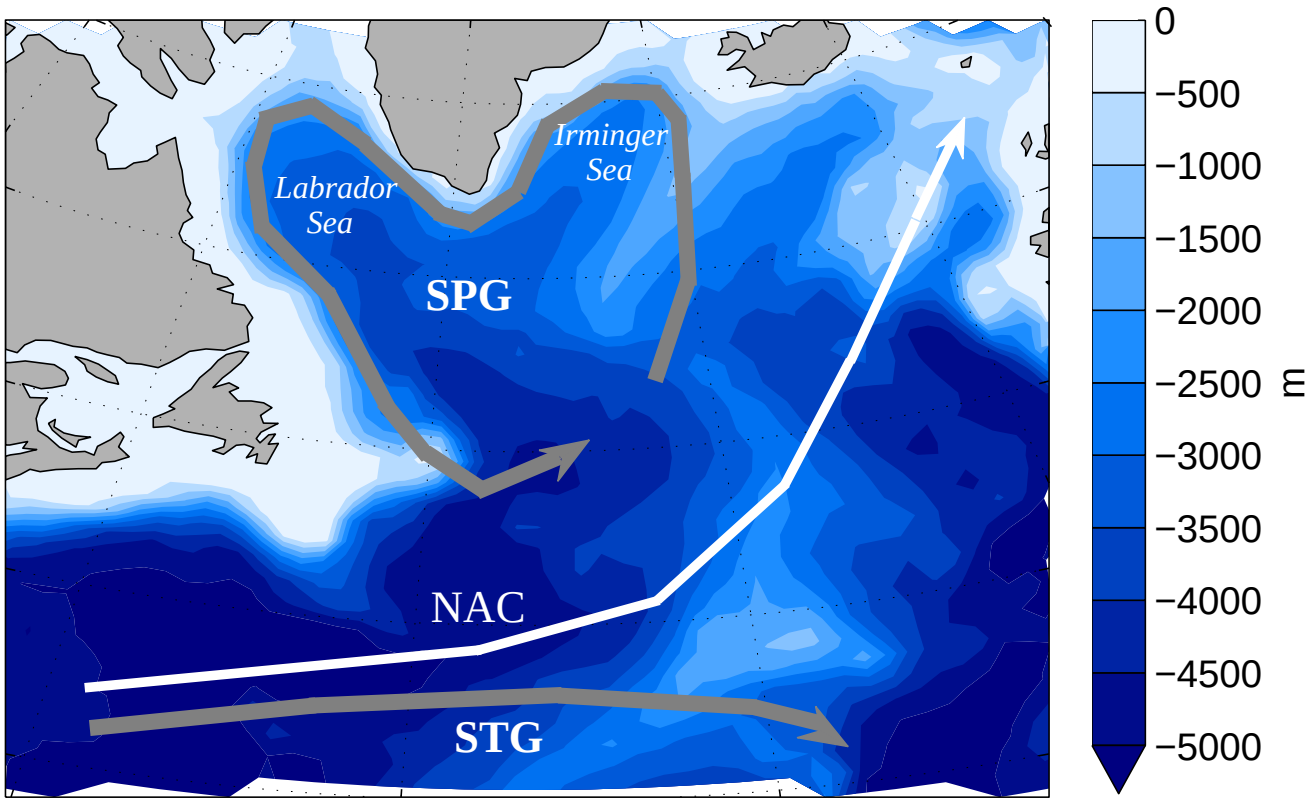

Figure 2.1: Bathymetry of the subpolar region in the North Atlantic. Arrows indicate circulation directions of the SPG and STG. The white arrow indicates the direction of the NAC.

warm and saline waters. They suggested that the trigger of the thinning and retreat of the Jakobshavn Isbræ was an increase in subsurface waters along the west coast of Greenland during the latter half of the 1990s. The driving mechanism behind this event is understood to be associated with the wind pattern over the SPG.

2.2 The North Atlantic Oscillation

The atmospheric wind pattern located over the North Atlantic is dominated by the westerlies which is confined to the region between the cyclonic low pressure system of high northern latitudes and the anticyclonic high pressure system in the subtropical Atlantic (Hurrell et al., 2003). Through the interplay between the ocean and atmosphere, vari-

ations in these westerly winds have large impact on the climate of the North Atlantic, as well on human activities and ecosystems.

The North Atlantic Oscillation (NAO) is an index that describes the strength of the westerlies (Hurrell et al., 2003). It involves a difference in Sea Level Pressure (SLP) between the centers of the North Atlantic subpolar low and subtropical high. During positive NAO index, this difference will be larger than normal with, in general, an anomalously low SLP close to Iceland and an anomalously high SLP close to the Azores. As a consequence, the westerlies intensify, resulting in enhanced wind speed associated with more numerous and intense storms in the North Atlantic, as well a northeastward shift of the storm paths. In addition, warm and moist air moves into the northeastern Atlantic while cold air from Greenland and northeastern Canada moves southward into the northwest Atlantic.

Based on monthly mean SLP data (1821-2000) provided by Phil Jones, Climatic Research Unit (CRU), University of East Anglia, Furevik and Nilsen (2005) demonstrated that the maximum and minimum SLP in the Icelandic region occur in May and January, respectively, while the SLP in the Azores region occur in opposite phase with maximum in January and minimum in May. Thus, there will be a much larger SLP difference during winter when the subpolar low is anomalously low and the subtropical high is anomalously high. This explains the large seasonal variations in the NAO and the strong seasonal dependency of the westerlies.

Studies have documented an eastward shift of the centers of maximum SLP anomalies in recent decades (Hilmer and Jung, 2000; Furevik and Nilsen, 2005). Hurrell et al. (2003) also report differences in the positions between the different NAO regimes, where the northern center is extended northeasteward during the positive NAO regime. Thus, the positions of the centers of action should not be considered to be at fixed geographic locations.

There are several ways of defining the NAO index. One of the most common methods is to use station based SLP differences between Lisbon, Portugal, and Stykkisholmur, Iceland (Hurrell, 1995). In this thesis an Empirical Orthogonal Function (EOF) analysis is used to extract the largest variability in the SLP data from the region 90 °W–30 °W and 20 °N–80 °N. The leading principal component (PC1) and spatial pattern obtained from

this analysis will be presented. An EOF based index will have larger spatial domain of influence on the mode of variability, compared to a simple two station based index (Furevik and Nilsen, 2005). This means that variability somewhere in the domain, which is not necessarily linked with the strength of the westerlies, will influence the pattern in other areas of the domain. In addition, extending an existing time series with new data will cause the EOF pattern and associated NAO index to change.

2.3 Atmospheric forcing

2.3.1 Heat and fresh water fluxes

The dominant pattern in the northern North Atlantic during positive NAO index is enhanced surface winds and surface cooling through sensible and evaporative heat fluxes (Visbeck et al., 2003). The ocean, with its large heat capacity and wet surface is the major source of heat and water vapor for the atmosphere (Hartmann, 1994, p. 171). The net heat flux, Q_{net} (W m^{-2}), through the sea surface consists of four components (Marshall and Plumb, 2008, p. 225):

$$Q_{net} = Q_{SW} + Q_{LW} + Q_S + Q_L, \tag{2.1}$$

where Q_{SW} (W m^{-2}) is the incoming shortwave solar radiation that is not reflected by the clouds, ocean surface or sea ice, and Q_{LW} (W m^{-2}) is the net flux of longwave radiation emitted from the ocean.

The two largest flux anomalies in the SPG, the sensible, Q_S (W m^{-2}), and latent, Q_L (W m^{-2}) (Visbeck et al., 2003), heat fluxes depend strongly on the surface wind speed. They can be expressed as in Hartmann (1994, p. 101):

$$Q_S = c_p \, \rho_a \, C_{DH} \, U_r \, \big(T_o - T_a(z_r)\big) \tag{2.2}$$

$$Q_L = L \, \rho_a \, C_{DE} \, U_r \, \big(q_o - q_a(z_r)\big), \tag{2.3}$$

where ρ_a (kg m^{-3}) is the air density, c_p (J kg^{-1} K^{-1}) is the specific heat at constant pressure, L (J kg^{-1}) is the latent heat of vaporization, and C_{DH} and C_{DE} are aerodynamic transfer coefficients for temperature and humidity, respectively. Equations (2.2) and (2.3)

shows that the sensible and latent heat fluxes relates to the difference between the sea surface temperature and the air temperature, $T_s - T_a(z_r)$ (K), and difference between the sea surface specific humidity and the air specific humidity, $q_s - q_a(z_r)$ (ratio of mass of water vapor per unit mass of dry air), respectively, as well the mean wind speed, U_r (m s^{-1}), at the reference height, r (m).

The net fresh water flux, F (km^3), between the atmosphere and ocean can be written

$$F_{net} = P + E, \tag{2.4}$$

where P is the precipiation and E is the evaporation (Large and Yeager, 2009). The freshwater budget of the ocean also include the river runoff into the ocean from the continents as well the horizontal ice transport carried with the ocean currents.

2.3.2 Ekman transport

In addition to the net heat and freshwater fluxes at the atmosphere-ocean interface, there may also be a horizontal heat or freshwater flux associated with the Ekman transports (Furevik and Nilsen, 2005). The turbulent response to wind forcing is limited to the Ekman layer, where the wind stress decays to zero at the lower boundary of the Ekman layer, which is called the Ekman depth (Marshall and Plumb, 2008, p. 200). In this layer, wind creates a net flow that is directed 90° to the right of the wind direction (northern hemisphere), which is expressed as

$$M_{ek} = \frac{\tau \times \hat{\mathbf{z}}}{f}. \tag{2.5}$$

Here M_{ek} (kg m^{-2} s^{-1}) is the lateral mass transport over the Ekman layer, known as the Ekman transport, $\hat{\mathbf{z}}$ indicate the unit vector directed normal and outward relative to the near surface of the ocean, and f (s^{-1}) is the Coriolis paramter. The wind stress, τ (N m^{-2}), can be estimated as in Thorpe (2007, p. 204):

$$\tau = \rho_a C_{Da} W_{10}^2, \tag{2.6}$$

where C_{Da} is the drag coefficient and W_{10} (m s^{-1}) is the wind speed at a height of 10 m which exert a stress on the ocean surface. The large scale wind stress pattern is defined as the wind stress curl, $\hat{\mathbf{z}} \cdot \nabla \times \frac{\tau}{\rho_a f}$ (N m^{-2}). Positive wind stress curl is analogous with

positive relative vorticity, $\zeta > 0$, meaning a cyclonic wind pattern, and negative wind stress curl, $\zeta < 0$, indicate anticyclonic wind pattern, where $\zeta = \frac{\partial v}{\partial x} - \frac{\partial u}{\partial y}$ (s^{-1}). The Ekman transport is convergent and divergent for anticyclonic and cyclonic wind stress curl, respectively.

The wind stress curl trend reflects the NAO variability, where positive NAO forcing is often related to an anticyclonic wind stress curl anomaly in the SPG (Häkkinen and Rhines, 2004). In addition, the anticyclonic wind stress curl in the STG during positive NAO is found to extend further into the northeastern North Atlantic, which lead to the extension of STG into the SPG region (Lohmann et al., 2008).

2.3.3 Sea Surface Height

The SPG region is characterized by relative cold and low-saline subarctic water (Hatun et al., 2009). Changes in the atmospheric forcing will affect the local heat and fresh water storage in the water column through the relations stated above. As a consequence, changes in the density, which is a function of temperature, salinity and pressure through the equation of state, will affect the sea surface height (SSH) (Häkkinen and Rhines, 2004). The equation of state can be approximated as in Thorpe (2007, p. 20):

$$\rho = \rho_{ref}(1 - \alpha_T T + \beta_S S), \tag{2.7}$$

where ρ is the density governed by small variations in the temperature, T, and salinity, S, from reference values for which the density is ρ_{ref}. In the above expression, variation in pressure have been neglected as these are minor in the upper 500-1000 m of the water column. The coefficients α_T and β_S are the thermal expansion and saline contraction coefficients, defined as $\alpha_T = -\frac{1}{\rho_{ref}}\frac{\partial \rho}{\partial T}$ (K^{-1}) and $\beta_S = \frac{1}{\rho_{ref}}\frac{\partial \rho}{\partial S}$ (psu^{-1}), respectively (Marshall and Plumb, 2008, pp. 166-167). The relation between the expansion/contraction of water columns due to changes in density is knwon as the steric effect. It's magnitude can be estimated following Marshall and Plumb (2008, pp. 186-187):

$$\frac{\Delta\eta}{H} \simeq \big(\alpha_T \langle T - T_0 \rangle - \beta_S \langle S - S_0 \rangle\big), \tag{2.8}$$

where $\Delta\eta$ (m) is the change in SSH and H (m) is the depth of the water column or, alternatively, the depth over which T and S changes. The angle brackets describe the

mean vertical temperature and salinity anomalies $T - T_0$ (K) and $S - S_0$ (psu), integrated from the depth $Z = -H$ to the surface $Z = -\eta$:

$$\langle() \rangle = \frac{1}{(H + \eta)} \int_{-H}^{\eta} () dz \tag{2.9}$$

2.3.4 Convective mixing

A change in density will also influence the bouyancy, b (m s^{-2}), and convection in the water column. The bouyancy can be defined as in Marshall and Plumb (2008, pp. 34-35):

$$b = -g \frac{(\rho_P - \rho_E)}{\rho_P}, \tag{2.10}$$

where ρ_P is the density of a water parcel, ρ_E is the density of the environment and g (m s^{-2}) is the gravitational acceleration. If $\rho_P < \rho_E$ then the buoyancy is positive and the parcel will rise, if $\rho_P > \rho_E$ the buoyancy is negative and the parcel will sink, and if $\rho_P = \rho_E$ the parcel is neutrally buoyant and is at rest. The reduced gravity g' is equal to the buoyancy b, but for opposite sign.

2.3.5 Mixed layer

Apart from the vertical Ekman transport which involves the ventilated isopycnals below the base of the Ekman layer, mechanical mixing takes place in the uppermost part of the water column where the actions of the overlying atmosphere lead to an almost uniform density profile, known as the mixed layer (Thorpe, 2007, p. 23). This layer plays an important role in storing heat and momentum from the atmosphere, with a thermal capacity of about 30 times the heat capacity of the atmosphere (Hartmann, 1994, p. 179). Large seasonal variations in wind speed and buoyancy forcing causes the mixed layer depth to vary from values reaching tens of meters to a few hundreds meters, with late winter and summer having maximum and minimum mixed layer depth, respectively.

2.4 Ocean circulation

2.4.1 Geostrophic flow

Horizontal variations in pressure at depth depends on the atmospheric pressure, the SSH, and variations in the vertical density stratification (Marshall and Plumb, 2008, p. 184). As will be verified in chapter 4, the SSH in the North Atlantic is higher in the STG than in the SPG. Such tilt in SSH is analogous with a pressure gradient generating geostrophic winds in the atmosphere. In the ocean, the equivalent to geostrophic winds can be derived by integrating the hydrostatic relation from a reference surface of constant depth z (m) to the SSH defined at $z = \eta$ (Marshall and Plumb, 2008, p. 183). The hydrostatic relation reads

$$\frac{\partial p}{\partial z} = -g\rho, \tag{2.11}$$

where $\frac{\partial p}{\partial z}$ is the change in pressure with depth (z increasing upwards). After neglecting near-surface density variations and day-to-day variations of atmospheric pressure, the surface geostrophic flow can be expressed as (Marshall and Plumb, 2008, p. 184)

$$\mathbf{u}_{g,surface} = \frac{g}{f}\hat{\mathbf{z}} \times \nabla\eta. \tag{2.12}$$

At depths greatly exceeding η, density variations cannot be neglected. The geostrophic flow where density variations are included becomes (Marshall and Plumb, 2008, p. 185)

$$\mathbf{u}_g = \frac{g}{f}\hat{\mathbf{z}} \times \nabla\eta + \frac{g(\eta - z)}{f\rho}\hat{\mathbf{z}} \times \nabla\rho. \tag{2.13}$$

The second term on the right hand side is associated with density variations in the ocean interior and act as a "thermal wind" term, implying that $\mathbf{u}_g$ will vary with depth. In the atmosphere, geostrophic wind increases with increasing height because isobars have similar orientation as potential temperature isolines. On the contrary, the ocean has, in general, compensating density gradients leading to baroclinic circulation at depth of opposite direction compared to the surface geostrophic flow. The latter follows directly from eq. (2.13): By assuming reduced $\mathbf{u}_g$ at depth, eq. (2.13) implies that

$$(\text{isopycnal slope in the ocean interior}) \propto -(\text{free surface slope})$$

where the proportionality factor is of the order 400 for the ocean (Marshall and Plumb, 2008, p. 186). Therefore, the internal isopycnals slope opposite to and are several hundred times steeper than the surface elevation.

2.4.2 Margules relation

During winter when the atmosphere cools the ocean, the density of the surface water increases followed by a lowering of the SSH. Consequently, the ocean buoycancy will be reduced and may trigger vertical mixing to the depth of an isopycnal layer of equal density.

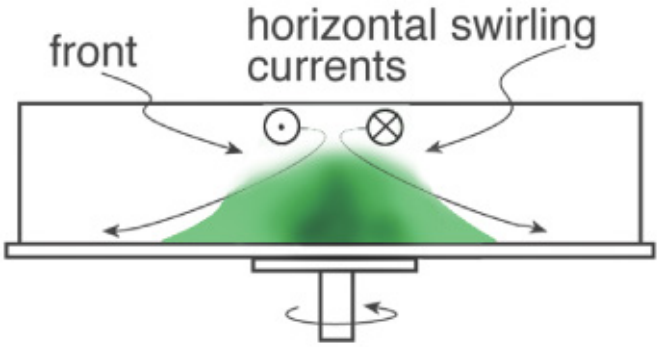

Figure 2.2: Illustration of a dense fluid (green) in the center of a rotating tank. The $\odot$ and $\otimes$ indicate the direction out of and into the paper plane, respectively, of the strong flow in the upper-level. Figure from Marshall and Plumb (2008, p. 124).

Figure 2.2 shows the creation of a dome of dense fluid collapsing under the combined effect of gravity and rotation. A domed structure in the ocean is created accordingly when convection (or any form for water mass transformation leading to increased density) increases the thickness of the isopycnals at intermediate depths (Häkkinen and Rhines, 2004; Lohmann et al., 2008). This structure is maintained by the balance between the gravitational pull represented by g' and rotation represented by f. This balance prevent the water from generating a dense fluid evenly distributed at the bottom, which would be the end-result for a non-rotating system. The balance is known as the Margules relation (Marshall and Plumb, 2008, p. 125),

$$v_{g1} - v_{g2} = -\frac{g' \tan\gamma}{f}. \tag{2.14}$$

Here γ denotes the slope of the interface between the two fluids in Fig. 2.2. $v_{g1} - v_{g2}$ (m s^{-1}) is equivalent to the baroclinic component on the right hand side of eq. (2.13), which act as a thermal wind term. Thus, for an idealised two-layered ocean with fluid 1 overlaying fluid 2, with densities $\rho_2 > \rho_1$ as illustrated in the right panel in Fig. 2.3, $v_{g1} - v_{g2}$ will be the difference between the geostrophic flow associated with the surface

elevation $\eta_1(x)$ and the geostrophic flow at depth. For small γ, $\tan\gamma \approx \gamma$. Therefore, eq. (2.14) can be expressed as

$$v_{g1} - v_{g2} = -\frac{g'}{f}\gamma. \tag{2.15}$$

As already mentioned, compensating density gradients lead to weaker geostrophic flow at depth such that $v_{g1} - v_{g2} > 0$. In addition, the deep flow will, in general, be less energetic than the near-surface flow because of radial expansion (due to conservation of angular momentum) and increased friction towards the bottom. Equation (2.15) shows that the velocity difference of the flow increases as the angle of the front sharpens and/or for increased density differences. In the ocean, a steepening of the domed structure is associated with a stronger circulation (Häkkinen and Rhines, 2004; Lohmann et al., 2008). This implies an increase in the v_{g1} component in eq. (2.15), which is consistent with an increase in the geostrophic flow in the upper ocean.

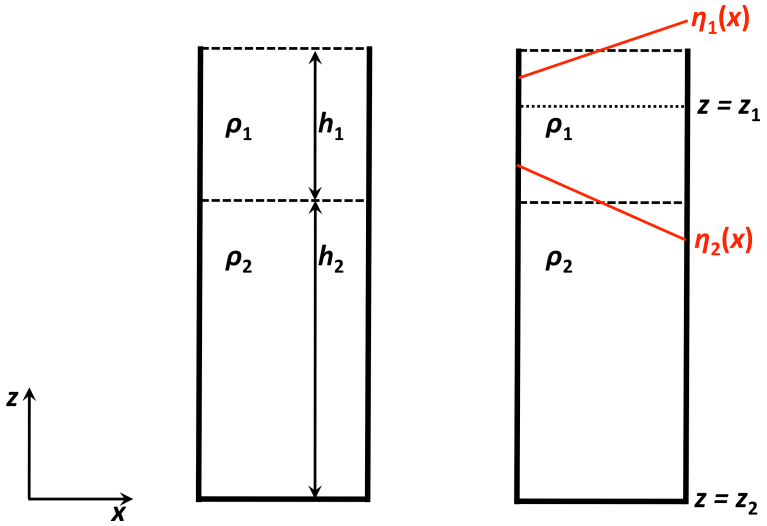

Figure 2.3: Illustration of a two-layered water column in a rotating frame. h_1 and h_2 indicate the height of the two fluids with densities ρ_1 and ρ_2, respectively, for an equilibrium state (left panel). The sloping interfaces are expressed in terms of $\eta_1(x)$ and $\eta_2(x)$ for the rotating frame (right panel). x and z denote the upward and eastward directions, respectively.

2.4.3 Barotropic streamfunction

In the ocean, the vertically averaged flow is known as the barotropic flow, which is the component of the total flow that occurs when the isobaric and isopycnal levels are parallell in the ocean (Stewart, 2008, p. 163). In contrast, the baroclinic flow component

in eq. (2.13) is associated with density gradients that are inclined to isobaric levels. The barotropic streamfunction is found by solving an elliptic partial differential equation (M. Bentsen, pers. comm., 2013) involving the x- and y-components of the mass fluxes $\mathcal{U} = \int u\,dp/g$ and $\mathcal{V} = \int v\,dp/g$ integrated from the bottom to the surface. The mass fluxes are related to the barotropic streamfunction ψ as follows:

$$\mathcal{U} = \frac{\partial \psi}{\partial y}, \quad \mathcal{V} = -\frac{\partial \psi}{\partial x} \tag{2.16}$$

An elliptic equation for the streamfunction can than be expressed as

$$\frac{\partial^2 \psi}{\partial x^2} + \frac{\partial^2 \psi}{\partial y^2} = -\Omega, \tag{2.17}$$

where the vorticity $\Omega = \partial \mathcal{V}/\partial x - \partial \mathcal{U}/\partial y$ has been introduced.

2.4.4 Vertical mixing

The mixing in the ocean is driven by turbulence, convection, diffusion, tidal and internal waves, and Ekman pumping/suction. The latter is a result of the divergence of the Ekman layer transport associated with the sign and magnitude of the wind stress curl (Marshall and Plumb, 2008, p. 204). The vertical velocity, ω_{ek} (m s^{-1}), at the bottom of the Ekman layer can be derived using eq. (2.5),

$$\omega_{ek} = \frac{1}{\rho_{ref}} \nabla_h \cdot M_{ek}, \tag{2.18}$$

where convergent flow drives downwelling (Ekman suction), while divergent flow drives upwelling (Ekman pumping).

The wind stress curl does also affect the depth-integrated circulation of the ocean,

$$\beta V = \frac{1}{\rho_{ref}} \hat{\mathbf{z}} \cdot \nabla \times \tau, \tag{2.19}$$

which is known as the Sverdrup relation (Marshall and Plumb, 2008, p. 213). Equation (2.19) relates the vertically integrated meridional transport V (m^{-2} s^{-1}), defined as $V = \int_{-D}^{0} v\,dz$ (D (m) is the ocean depth), to the wind stress curl. Zero wind stress curl mean that $V = 0$ and $\omega_{ek} = 0$, which defines the boundary between ocean gyres.

2.5 Atlantic Meridional Overturning Circulation

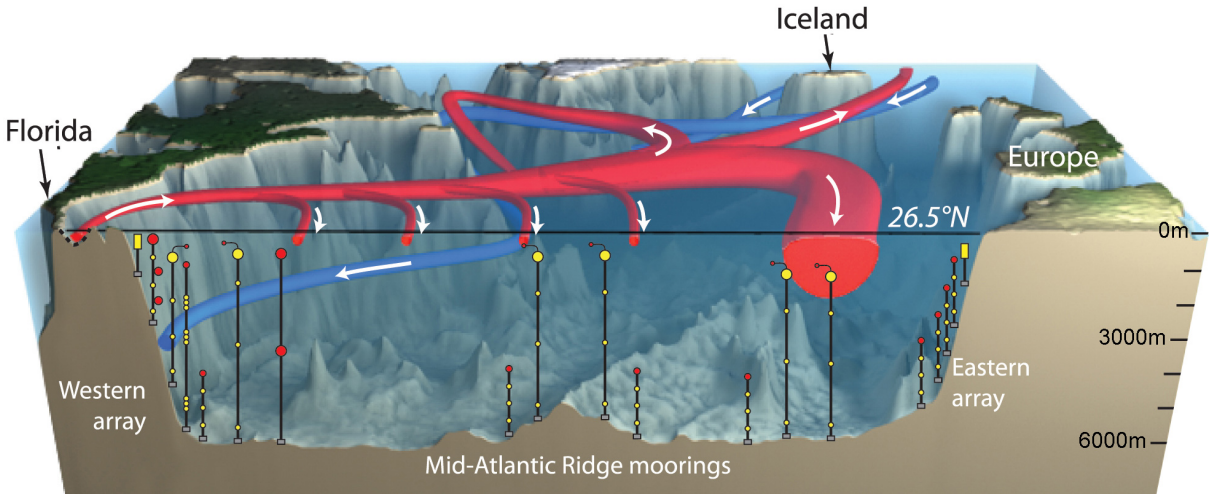

Figure 2.4: Diagram of the AMOC indicated by warm ocean currents (red) and cold and dense ocean currents (blue). The black lines with yellow and red circles indicate moorings placed across the Atlantic at 26.5°N. The figure is obtained from http://www.rapid.ac.uk/rw/news.php#n15.

The Atlantic meridional overturning circulation (AMOC), illustrated in Fig. 2.4, is a commonly used quantity describing the balance between the northward heat transport of subtropical origin (red colour) and the deep southward return flow (blue colour). At 26.5°N, the Atlantic Ocean heat transport is close to its maximum, providing 70% of the net poleward heat transport carried by the gobal oceans (Johns et al., 2011). Heat loss to the atmosphere increases the density of the northward flow at high latitudes, where the water masses undergo a gradual densification and descend in the water column and return southward (Eldevik et al., 2009). The formation of dense water in the SPG and the Nordic Seas during strong atmopsheric forcing lead to a spin up of the AMOC (Lohmann et al., 2008). Consequently, increasing amount of intermediate to deep water masses will eventually flow southward from the convective regions. To compensate the southward dense flow, more warm and saline waters of subtropical origin enters the SPG.

In chapter 4, both the monthly maximum strength of the AMOC at 26.5°N and 41°N will be presented. 41°N is typically near the region where the AMOC reaches its maximum strength (Talley et al., 2011, Fig. 14.8).

2.6 Labrador Sea deep convection

As Visbeck et al. (2003) demonstrates, the Labrador Sea is a major convective region which directly affects the strength of the SPG circulation and AMOC. Formation of intermediate to deep water masses in this region depends on the season and NAO forcing, going from high NAO index with strong convection to low NAO index when heat loss is low and deep convection is reduced. In addition, poleward heat transport, changes in ocean circulation, mixing with shelf waters and fresh water transport from the Arctic alters the heat and fresh water storage in the Labrador Sea, which affects the buoyancy (Visbeck et al., 2003).

A severe winter will extract more buoyancy than what is received during the preceeding summer, which results in less buoyancy to be removed the following winter (Lazier et al., 2002). Consequently the deep convection in the following winters can proceed, typically reaching to greater depths, which is different from convection that is limited by a single winter's heat loss where all buoyancy is replaced during the summer.

2.7 The mid 1990s regime shift in the SPG

As described above, variations in the strength of the SPG and associated influences on the northern North Atlantic climate is linked with the NAO. Between the early 1960s and mid 1990s the SPG was generally experiencing cool conditions where advective heating of the SPG region was largely counterbalanced by strong surface cooling (Yeager et al., 2012). The climate during this period was associated with a relative high NAO index, which led to strong air-sea fluxes and a well-established gyre circulation. After the winter 1995/96, the SPG was followed by anomalously warm conditions. This 1995-1996 switch in SPG strength, going from a cool and strong gyre circulation to an abrupt change towards warm and weak gyre circulation has been examined by Lohmann et al. (2009). They concluded that the change was inevitable because of several years with very strong positive NAO forcing, which spun up the SPG and subsequently the AMOC. Consequently, advection of STG water into the SPG region increased, which counteracted the cooling effects from the positive NAO forcing. The net result was reduced production

of intermediate to deep water masses and eventually relaxation of the doming structure of the SPG. In addition, the NAO forcing went from strong positive to strong negative values in the winter 1995/96, which amplified the inevitable weakening of the SPG.

The switch in SPG strength after persistent positive NAO forcing is important since it explains a non-linear interplay between the ocean state and atmospheric forcing (Lohmann et al., 2008). In contrast, the ocean response to a persistent negative forcing shows a linear relationship with the atmospheric forcing, with a steady weakening of the SPG until a minimum value is reached.

There is a potential that the North Atlantic climate can be predicted up to 10 years in advance (Collins et al., 2006). If a climate model should be able to conduct decadal predictions of the North Atlantic, basic mechanisms and naturally occurring variations in the marine climate must be understood and simulated by the model. Based on a newly developed version of the Bergen isopycnic OGCM, analyzes of ocean conditions from the period 1960-2008 will be investigated and attempted to be put into the framework of this chapter.

Chapter 3

The ocean component of the Norwegian Earth System Model

The Norwegian Earth System Model (NorESM) is a numerical climate model which utilizes atmospheric, land, sea-ice and ocean components to simulate Earth's climate. It is an coordinated effort mainly developed at the Bjerknes Centre for Climate Research in Bergen, the Norwegian Meteorological Institute in Oslo and the Department of Geosciences at the University of Oslo (Bentsen et al., 2013; Iversen et al., 2013). The analysis in this thesis is based on model simulations from the ocean component of NorESM. This ocean component is an isopycnic OGCM, originating from the Miami Isopycnic Coordinate Ocean Model (MICOM (Bleck et al., 1992)) and developed further in Bergen.

3.1 Horizontal coordinates

Figure 3.1 shows the distribution of grid points in the ocean model. The horizontal resolution is approximately 1 degree, apart from an area between 20 °N-20 °S which has a finer resolution (Bentsen et al., 2013). Because of the spherical grid used in the model, the grid size will get smaller as the meridians converge towards the poles. To avoid numerical problems in the ocean domain and to allow for longer time steps, these polar singularities are mapped over Canada and Siberia using a coordinate transformation (Bentsen et al., 1999).

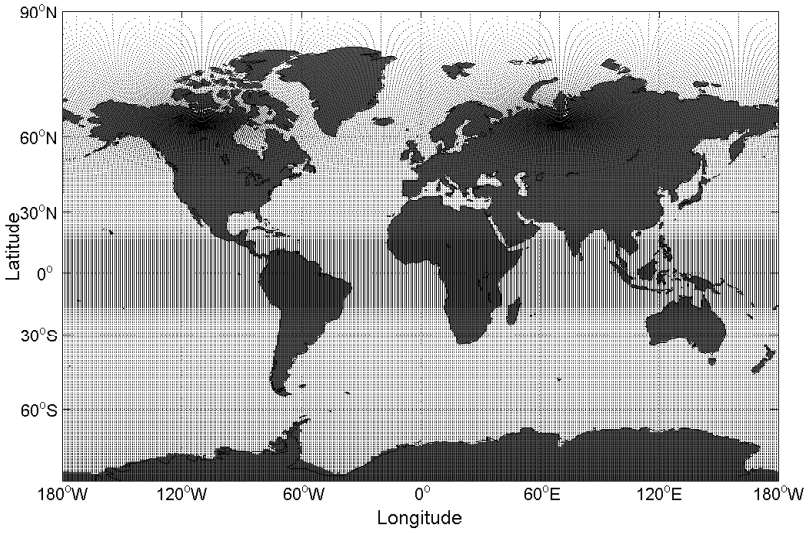

Figure 3.1: Curvilinear coordinate points shown as dots on a cylinder map projection. The grid cells are structured, which means they have the same number of sides and neighboring cells. Each grid cell is locally orthogonal to the neighboring cells.

The model uses the leap frog and forward-backward time stepping explicit schemes for the barotropic and baroclinic modes, respectively (Bentsen et al., 2013). Generally, the stability of these schemes are limited by

$$\frac{c\Delta t}{\Delta x} \leq 1, \tag{3.1}$$

which is known as the so-called Courant Friedrichs Lewy (CFL) criterion (Press et al., 1992, p. 829). The CFL number ($C = c\Delta t/\Delta x$) depends on the time step Δt and the local grid size Δx as well the advection velocity c of the model's variables. To avoid instability, Δt must be kept sufficiently small.

The ocean model's equations are discretized on an Arakawa C grid staggering which is illustrated in Fig. 3.2. Each grid box contains a p, $\mathbf{q}$, $\mathbf{u}$ and $\mathbf{v}$ point within each grid cell as depicted in Fig. 3.2.

3.2 Vertical coordinate

The ocean component of the NorESM uses surfaces of constant potential density, i.e., isopycnal surfaces, as vertical coordinate (Bentsen et al., 2013). Mixing and tracer transport generally occur along isopycnal surfaces in the ocean (Griffies et al., 2000). Thus, an

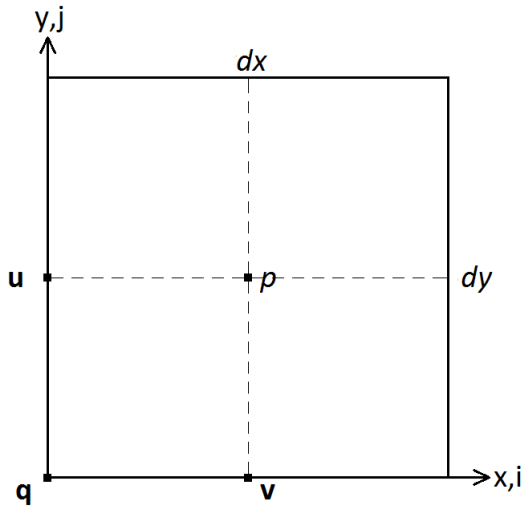

Figure 3.2: Model variables staggared on the horizontal Arakawa C grid. p refers to scalar values, **q** refers to functions or vectors of the horizontal components, **u** and **v**, in the x and y direction, respectively. dx and dy give the size of the grid cell.

Table 3.1: Model layer potential densities, expressed in σ_2-units, which is the potential density-1000 ($\mathrm{kg\,m^{-3}}$), referenced to 2000 dbar.

Layer	σ_2	**Layer**	σ_2	**Layer**	σ_2	**Layer**	σ_2	**Layer**	σ_2	**Layer**	σ_2
1	27.220	10	31.477	19	34.900	28	36.497	37	37.022	46	37.327
2	27.720	11	31.920	20	35.172	29	36.584	38	37.060	47	37.358
3	28.202	12	32.352	21	35.417	30	36.660	39	37.096	48	37.388
4	28.681	13	32.772	22	35.637	31	36.728	40	37.131	49	37.419
5	29.158	14	33.176	23	35.832	32	36.789	41	37.166	50	37.450
6	29.632	15	33.564	24	36.003	33	36.843	42	37.199	51	37.480
7	30.102	16	33.932	25	36.153	34	36.893	43	37.231	52	37.580
8	30.567	17	34.279	26	36.284	35	36.939	44	37.264	53	37.800
9	31.026	18	34.602	27	36.398	36	36.982	45	37.295		

ocean model expressed in terms of isopycnal surfaces, with a small component normal to the isopycnals is, by construction, well suited for representing long-term dynamics in the ocean.

The model's isopycnal surfaces ability to reflect the stratification in the ocean depends on

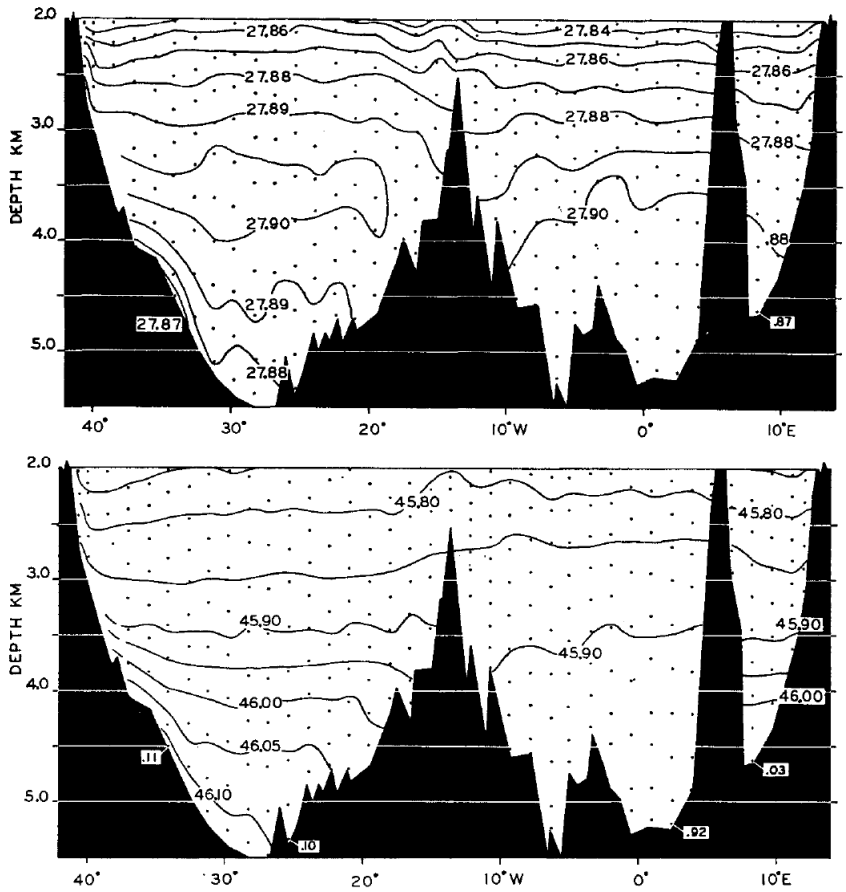

Figure 3.3: Potential density at depths greater than 2000 m, referred to zero dbar in upper panel (contour interval is 0.01), and 4000 dbar in lower panel (contour interval is 0.05). The values are from a section along 24 °S in the Atlantic Ocean where South America is on the left, the Mid-Atlantic ridge in the middle, and the Walvis and Africa on the right. Panels are obtained from Lynn, 1971.

the choice of reference pressure (Lynn, 1971). In the OGCM used here, the model has 53 isopycnal layers ranging in potential density relative to 2000 dbar from $\sigma_2 = 27.22\,\mathrm{kg\,m^{-3}}$ to $\sigma_2 = 37.8\,\mathrm{kg\,m^{-3}}$, listed in table 3.1. A water parcel that is raised or lowered close to this referance pressure will experience a density stratification that accurately reflects the stratification of the ocean at that depth, while becoming less accurate at increasing intervals from this referance pressure (Lynn, 1971).

Figure 3.3 shows the potential density referred to a pressure of zero and 4000 dbar across the Atlantic Ocean at 24 °S. The potential density is a function of temperature and salinity. The lower panel shows much larger gradients and values since the potential density is based on a much higher pressure than the potential density in the upper panel. In addition, when water is adiabatically lowered to the bottom of the ocean where pressure is high, the compressibility effect of the water increases. The result is an

increase in the temperature dependency on density since the compressibility of water increases with decreasing temperature. Referred to 4000 dbar, potential density gives a good representation of the deep ocean stratification and circulation, while referred to zero dbar it is an identifier of water origin (Lynn, 1971). Thus, the choice of 2000 dbar as a reference pressure is a compromize between the above mentioned choices, with an adequate description of the stratification at intermediate depths.

3.3 Model spin up

Figure 3.4: Spin up cycles of the model. The fifth cycle is used in this thesis.

The model was spun up using four consecutive 60 year cycles representing the reanalysis field from the time period 1948-2008. Before the initial cycle was started, oberservation-based ocean temperature and salinity defined the ocean conditions in 1948, while the ocean is set to rest with preset sea ice extent and thickness. After initialization, the model was forced with daily reanalysis fields from the NCEP-NCAR based coordinated ocean-ice reference experiments 2 (CORE2) reanalysis (Griffies et al., 2012), where each initial ocean state is taken from the end state of the previous cycle (Fig. 3.4). After the 4th cycle, yielding a total spin up period of 250 years, the model has reached a quasi-equilibrium state. It is the fifth cycle which is analyzed here.

The MICOM version in this thesis is forced with the CORE2 data set described by Griffies et al. (2012). It is important that the sea ice model coupled to the ocean is realistic in the sense that sea ice melt and formation alter the thermohaline fluxes and buoyancy forcing, which affect the deep convection and large scale overturning circulation.

Chapter 4

Results

4.1 Global climatology

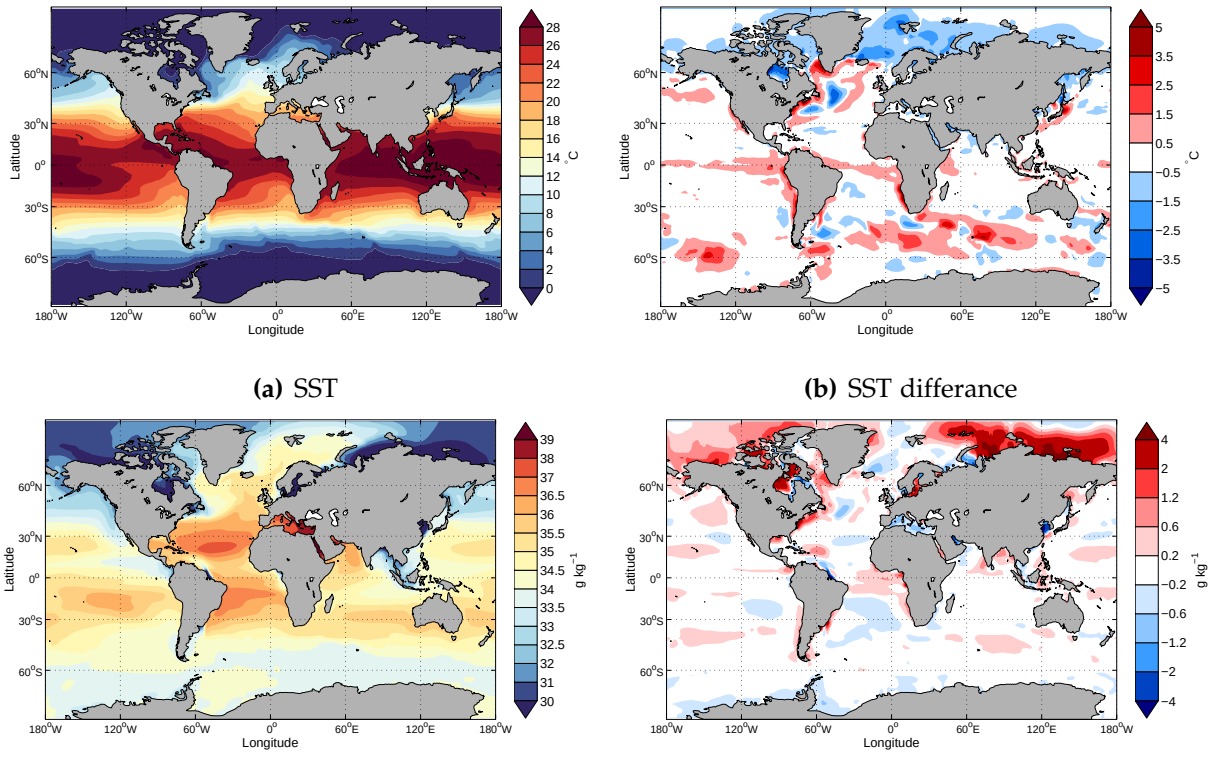

(a) SST

(b) SST differance

(c) SSS

(d) SSS differance

Figure 4.1: Left panels shows the mean simulated SST and SSS of years 1960-2008. Right panels show corresponding differance between simulated and observed data (model minus observations). The SST and SSS observation data is described in Locarnini et al. (2010) and Antonov et al. (2010), respectively, and obtained from http://www.nodc.noaa.gov/OC5/WOA09/woa09data.html.

Left panels in Fig. 4.1 displays the global sea surface temperature (SST) and salinity (SSS) averaged over years 1960-2008. Both SST and SSS in the northern North Atlantic show high values compared to other areas at similar latitudes. Differences between the simulated and observed values, the latter obtained from World Ocean Atlas 2009 (Antonov et al., 2010; Locarnini et al., 2010), are displayed in the right panels. They indicate that the model underestimates the temperature and salinity off New Foundland, while overestimates SST and SSS in the periphery of the SPG. In the Arctic region, cold and salt biases are, in general, found.

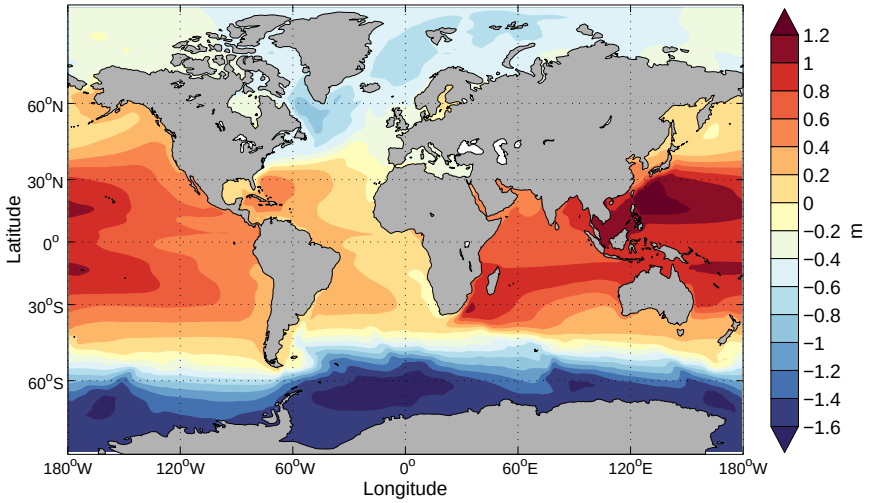

(a) SSH

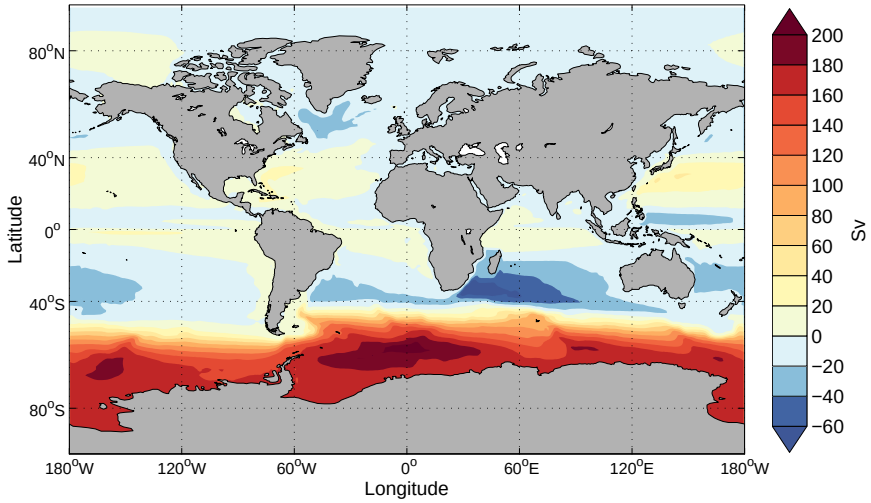

(b) Barotropic streamfucntion

Figure 4.2: Mean simulated SSH (relative to the global mean value) **(a)** and barotropic streamfunction **(b)** of years 1960-2008.

Figure 4.2 shows the global SSH and barotropic streamfunction averaged over the period 1960-2008. Figure 4.2(a) shows a strong tendency for elevated SSH at low and mid latitudes. The lowest SSH in the northern hemisphere is located in the SPG, with a minimum value of around –0.9 m relative to the global mean SSH. There is a distinct drop between 50-70 °S which contains the lowest global value of around –1.7 m. The barotropic streamfunction is shown in Fig. 4.2(b). The main features are positive streamfunction values in the subtropical oceans, and negative values in the subpolar oceans. At about 60 °S, the flow is mainly zonal because of the absence of continents and the presence of the Antarctic "island". At Drake Passage, the transport from the South-American to Antarctic continent ranges from 80-160 Sv, which is consistant with observational based estimates (Talley et al., 2011, pp. 451-452). There is a strong cyclonic flow in the SPG with a strength that is only exceeded by the cyclonic flow south of Madagascar. Notice that the two patterns show smiliarities in the SPG, as well between 40 °S and 80 °S, where a strong flow is almost identical with the negative SSH pattern in the same region.

4.2 NAO composites

Figure 4.3 shows the EOF analysis of SLP data from the NCEP-NCAR reanalysis using a singular value decomposition (SVD) to extract the leading mode of variability. The subpolar low and subtropical high is located west of Iceland and east of the Iberian Peninsula, respectively, with a difference in SLP of about 7 hPa. Notice the large drop in the PC1 during the winter 1995/96 which is unprecedented during the time period. The PC in Fig. 4.3(a) is shown as black bars in Fig. 4.4, and will be used as proxy for the NAO index throughout this thesis.

As mentioned in section 2.2, the NAO index describes the strength of the atmospheric forcing in the North Atlantic. In the process of describing how the ocean responds to different NAO values, three different NAO composites are derived which define the atomspheric forcing for a positive (NAO^+), a neutral (NAO^n) and a negative (NAO^-) NAO index. These composites are based on the years where the NAO values are highly positive, close to zero or highly negative, respectively, shown with red, green and blue symbols in Fig. 4.4. The years indicated by circles define the NCEP-NCAR composites

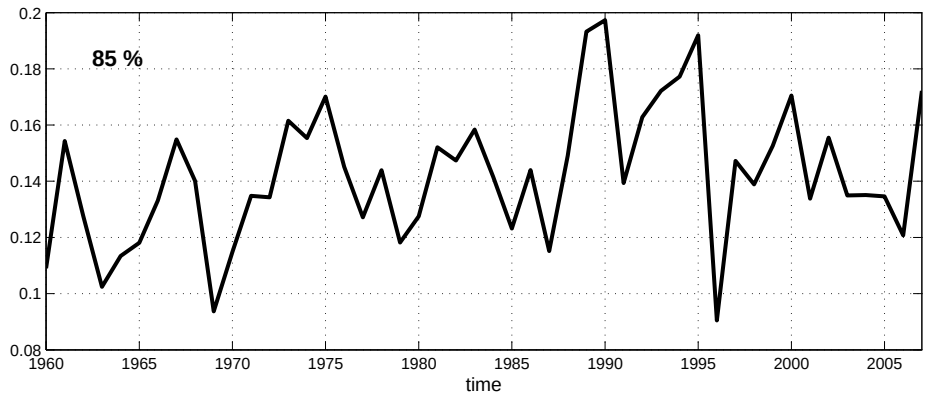

(a) PC1

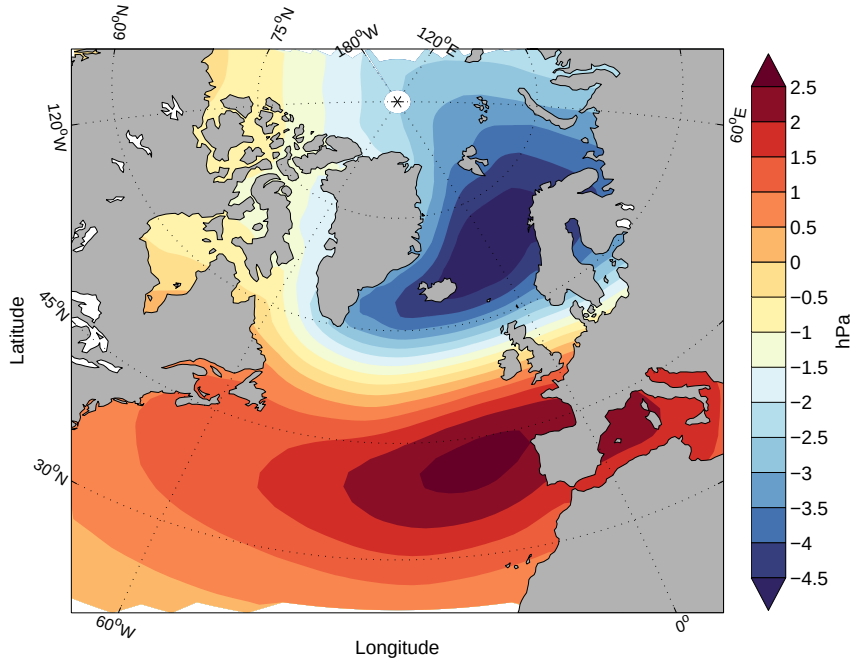

(b) NCEP-NCAR SLP data

Figure 4.3: **(a)** PC1 of the EOF analysis of winter mean (December-March) SLP data. The variance explained by the PC1 of the SLP data is given in the upper left corner. **(b)** Winter mean SLP data regressed on the normalized PC1. The SLP data used in the EOF analysis is the 1960-2008 NCEP-NCAR reanalysis data for the Atlantic sector 90 °W-30 °W and 20 °N-80 °N.

based on the NAO index shown as black bars. Years indicated by plus symbols define the ERA40 composites based on the NAO index in Lohmann et al. (2009). This NAO index is based on the ERA40 reanalysis defined as the difference of normalized winter SLP between Lisbon, Portugal, and Reykjavik, Iceland. The star symbols indicate those years which are common to both the NCEP-NCAR and ERA40 composites. The ERA40 NAO^+ and NAO^- composites are averages of years with standard deviation exceeding

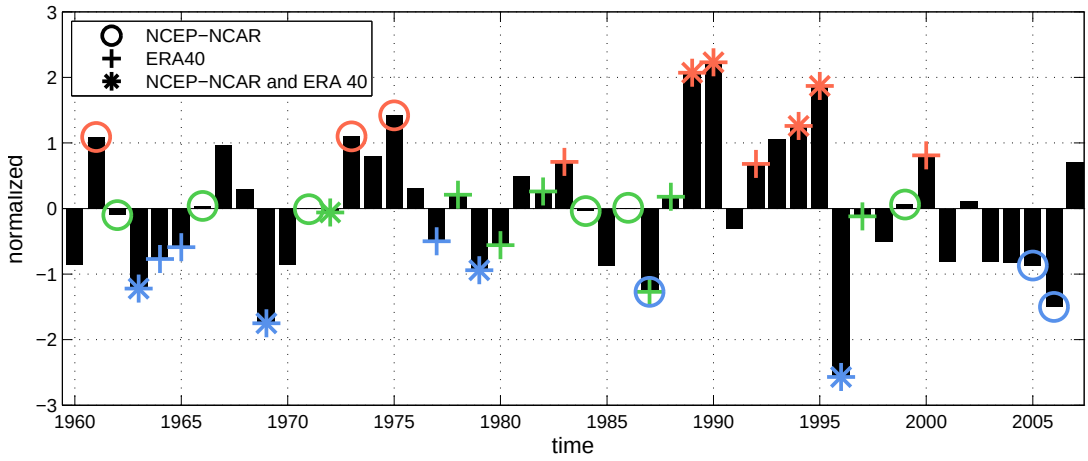

Figure 4.4: Winter NAO index based on the normalized PC1 from Figure 4.3(a). Bars marked with symbols indicate years which are used as NAO composites for the corresponding NAO index, where red values are positive, green are neutral and blue are negative NAO conditions.

unity larger and smaller than one, respectively. The NAO^n composite is based on the 7 years with lowest amplitude. Similarely, the NCEP-NCAR composites consists of the 7 years with largest positive, largest negative or smallest amplitude for the NAO$^+$, NAO$^-$ and NAO^n composites, respectively.

The two different methods for extracting the NAO index generate two NAO indices of different NAO values. This will generate two different sets of NAO composites where the NAO$^+$ and NAO$^-$ composites have 4 years in common (1989, 1990, 1994, 1995 and 1963, 1969, 1979, 1996, respectively), while the NAO^n composite only has 1 year in common (1972). In the following, differences between the two sets of NAO composites will be presented for different ocean properties, which to the best of the authors knowledge, have not been studied before. All time series will be averaged annualy unless otherwise stated. We define a year to start in July and end in the following June. This choice encompasses largest seasonal variability which, in our case, is the boreal winter. The year number is given by January of our boreal year.

4.3 Ocean response to atmospheric forcing

Figure 4.5 shows the SLP for NAO$^+$, NAO^n and NAO$^-$ composites. The ERA40 and NCEP-NCAR composites are displayed in the left and right panels, respectively. There is

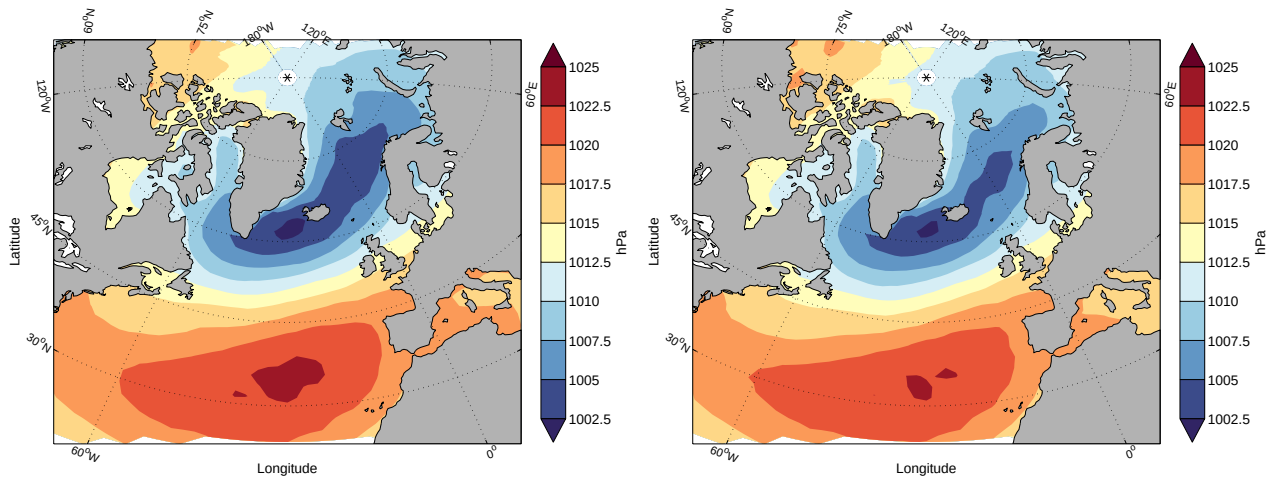

(a) NAO^{+}

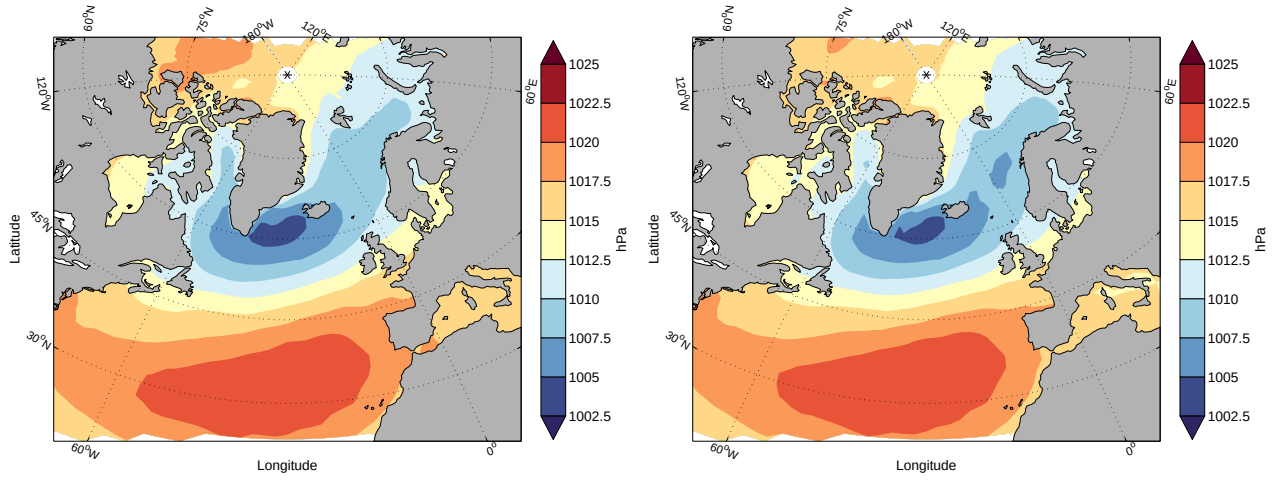

(b) NAO^{n}

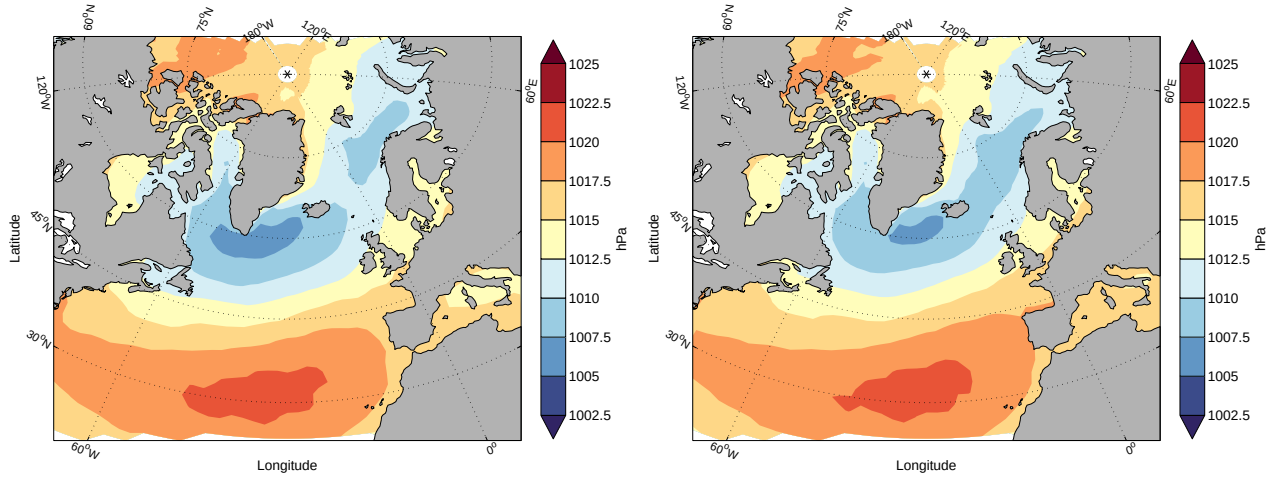

(c) NAO^{-}

Figure 4.5: ERA40 (left panels) and NCEP-NCAR (right panels) composites of SLP data from the NCEP-NCAR reanalysis.

a general agreement between the two sets of composites, where NAO^+ shows the largest amplitudes, followed by NAO^n and NAO^-. This pattern, describing the influence of the different NAO composites, is consistent with the pattern detected in the first mode of variability of the EOF analysis in Fig. 4.3.

Figures 4.6 and 4.7 show the SSH and the upper (400 m) ocean temperature and salinity response on the NAO^+ and NAO^- forcings relative to the NAO^n forcing, based on the ERA40 and NCEP-NCAR NAO composites, respectively. In this way, the different effect of strong and weak atmospheric forcing is compared to a neutral NAO state. In chapter 5, NAO^+ relative to NAO^- forcing will also be discussed. The reason for averaging the upper 400 m of the water column will be discussed below.

For the NAO^+ forcing, the SSH anomalies represent a dipolar pattern with anomalously low values in the SPG region and high values in large parts of the STG. The tilt of the SSH creates a geostrophic flow that is aligned along the boundary of the two gyres. The NAO^- forcing (right panels in Figs. 4.6 and 4.7) is largely opposite but with smaller amplitudes for the ERA40 composites, while the NCEP-NCAR version shows a negative anomaly in the central SPG.

The ocean temperature anomaly pattern shows the same dipolar pattern as the SSH. Negative anomalies indicate that the ocean temperature is lower relative to the NAO^n forcing, which is found in the SPG. The NAO^- forcing of the ERA40 composite also shows a opposite tendency of the NAO^+ forcing, while the NCEP-NCAR shows largely positive anomalies.

The ocean salinity depends on precipitation, evaporation, melting/freezing of sea ice, river runoff and Ekman induced fresh water flux which together form the net fresh water budget. The NAO^+ forcing shows anomalously high salinity located along the NAC for both sets of composites, while there is less agreement in the SPG region. The NAO^- forcing shows a negative anomaly south of the SPG for the ERA40 composite, while high salinity is located along the NAC and large parts of the SPG in the NCEP-NCAR composite.

The positive temperature and salinity anomalies seen along the NAC and STG for the NAO^+ forcing contribute oppositely to the SSH where positive temperature anomalies decrease the density and increase SSH, while positive salinity anomalies increase the

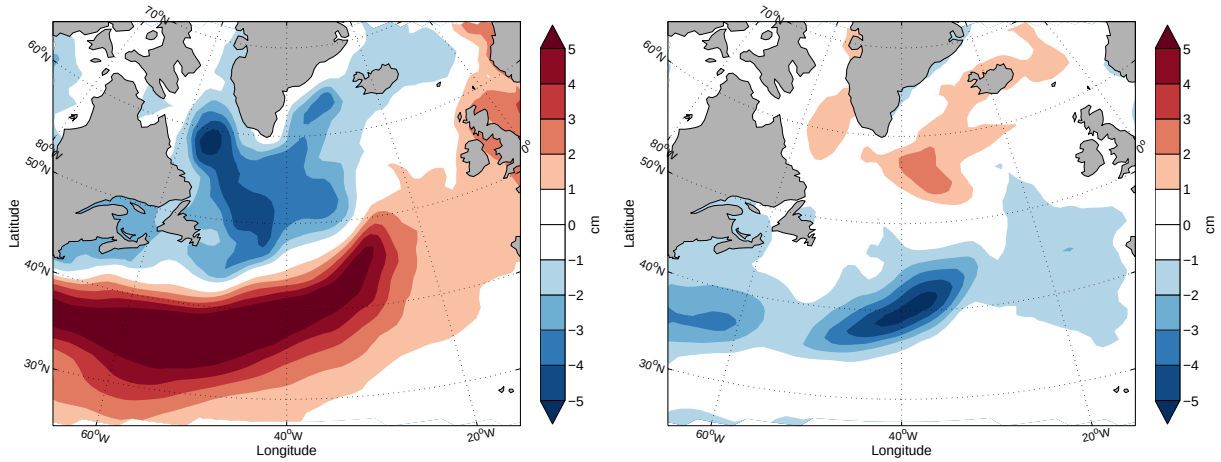

(a) SSH

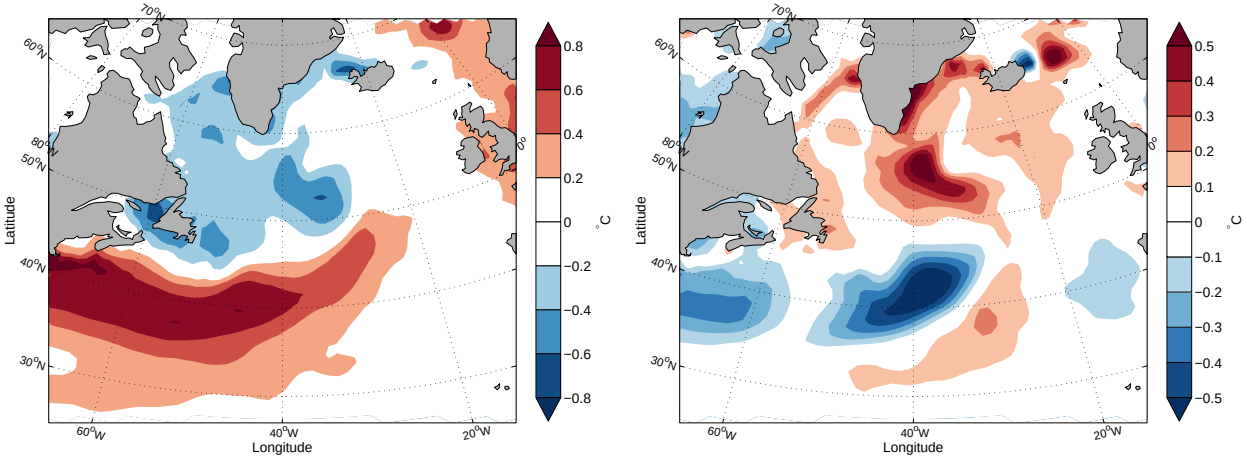

(b) OT

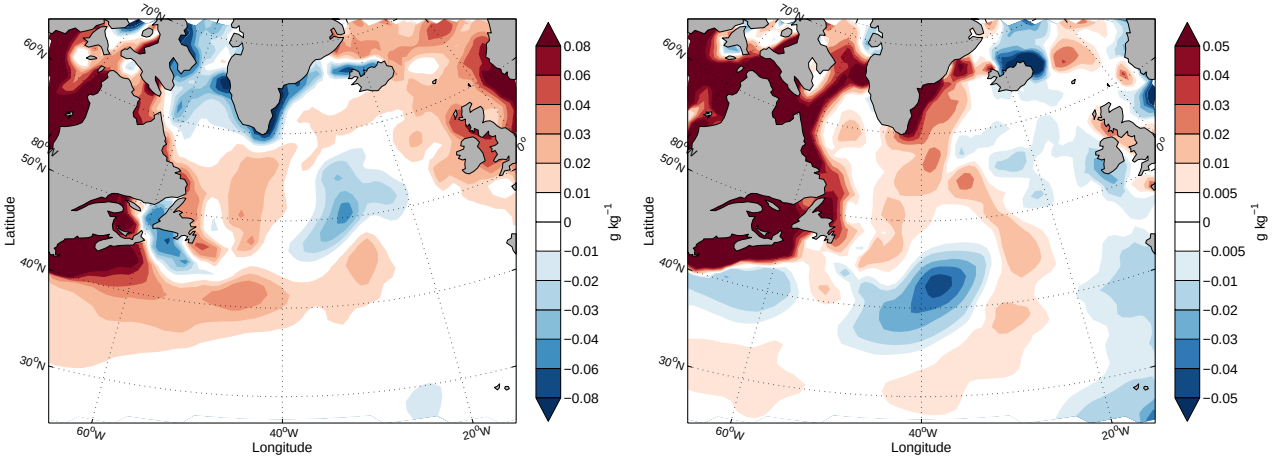

(c) OS

Figure 4.6: Difference in SSH, and vertically averaged ocean temperature (OT) and salinity (OS) for the upper 400 m of the water column between years with NAO^+ and NAO^n forcing (left panels), and NAO^- and NAO^n forcing (right panels). The NAO composites are based on the ERA40 NAO index.

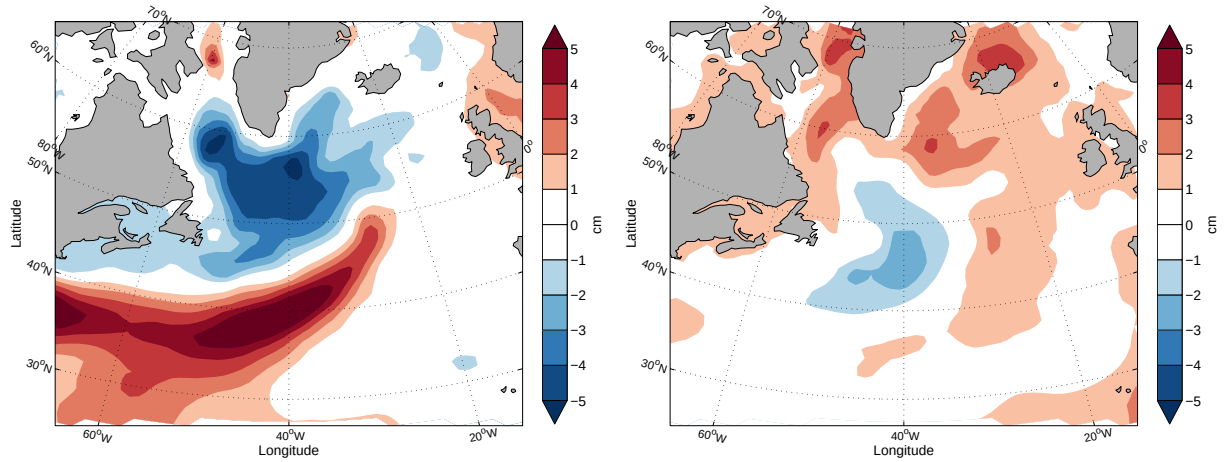

(a) SSH

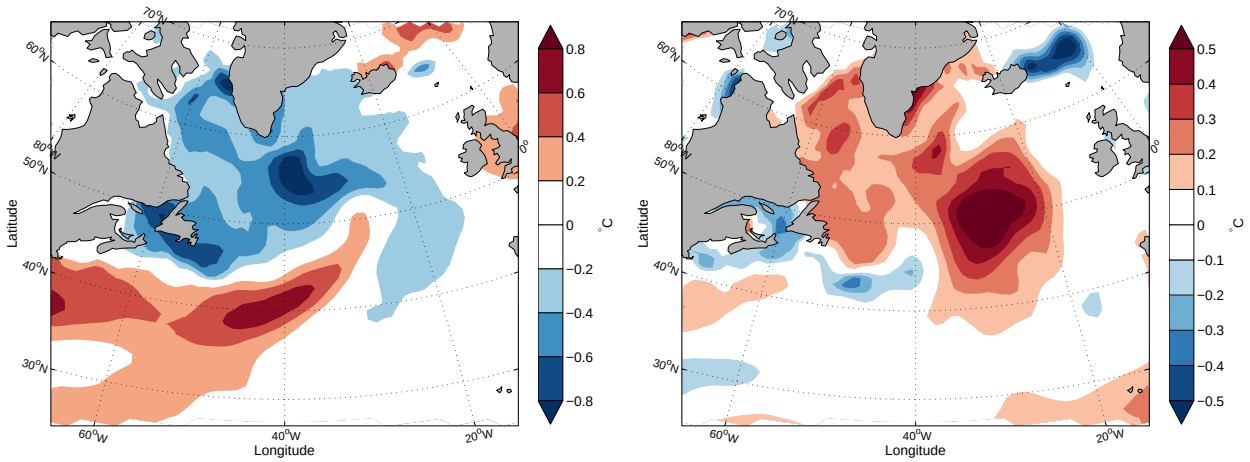

(b) OT

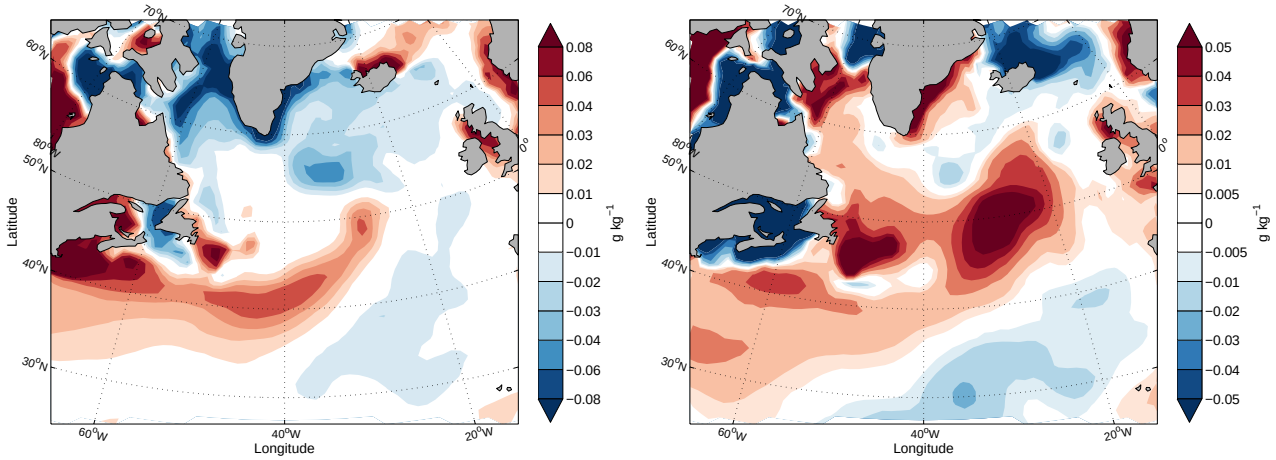

(c) OS

Figure 4.7: Same as Fig. 4.6, but NAO composites based on the NCEP-NCAR NAO index.

density and lowers SSH. Based on this, the steric effect from the thermal and haline anomalies act in opposite directions along the NAC and STG. Excluding the contribution

from below 400 m and the dynamic effects on the SSH, the most important contribution to SSH is temperature, with anomalies closely resembling the SSH pattern. This is in agreement with Lohmann et al. (2008, Fig. 8), which showed that changes in the steric height is dominated by the thermal contribution.

The main differences between the two sets of composites for the NAO^+ forcing are larger SSH and ocean temperature amplitudes along the NAC and STG for the ERA40 pattern, which indicate a larger ocean heat transport. Otherwise, a general agreement is seen for the NAO^+ forcing, while there is little or no consistency for the NAO^- forcing between the two sets of composites.

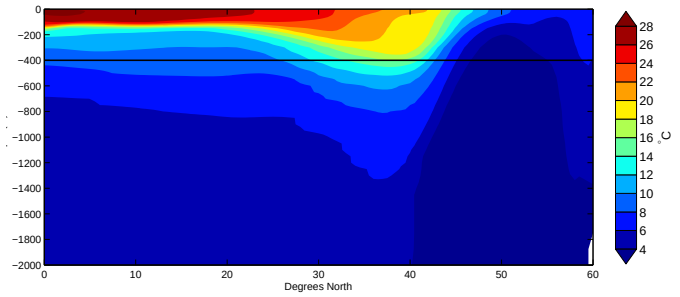

(a) Mean temperature

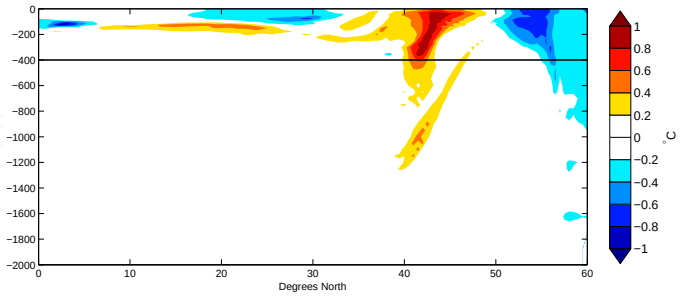

(b) NAO^+ – NAO^n of ERA40 composites

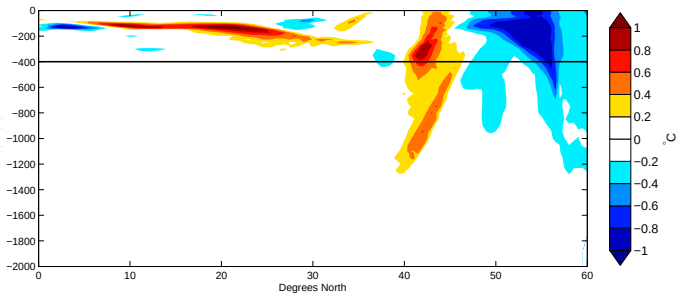

(c) NAO^+ – NAO^n of NCEP-NCAR composites

Figure 4.8: Mean temperature of year 1960-2008 **(a)** and difference in ocean temperature between years with NAO^+ and NAO^n forcing for the ERA40 composites **(b)** and NCEP-NCAR composites **(c)**. The values are from the transect along 0-60 °N at −40 °W. The black line represents –400 m depth.

Figure 4.8 displays the upper 2000 m of the water column along the transect 0-60 °N at −40 °W. Figure 4.8(a) shows the mean temperature for the period 1960-2008. Figures 4.8(b) and 4.8(c) shows the temperature difference between NAO^+ forcing relative to a neutral state, based on the ERA40 and NCEP-NCAR composites, respectively. The largest amplitudes are typically found in the upper 400 m of the water column in the STG (positive anomalies) and in the SPG (negative anomalies). Thus, the upper 400 m is choosen because this depth interval encompass the core of the seasonally ventilated STG and SPG water masses, and is directly influenced by the atmospheric momentum, heat and fresh water fluxes, which through convection and ekman pumping affects the deeper circulation. In chapter 5, the ocean temperature and salinity averaged in the upper 2000 m will also be discussed.

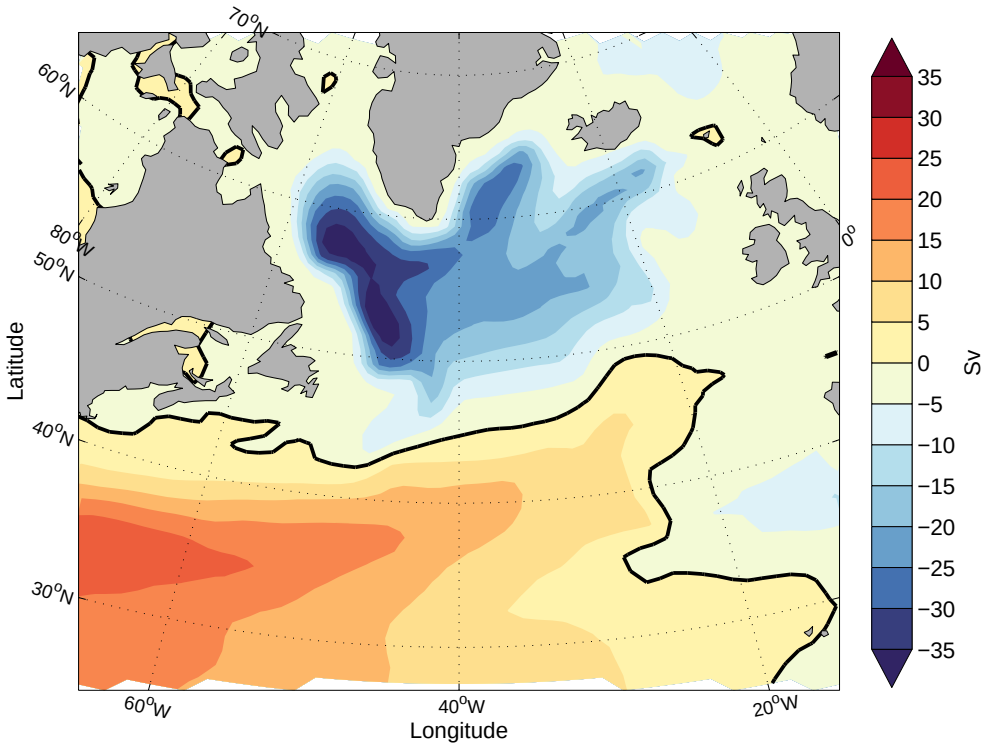

Figure 4.9: Mean barotropic streamfunction of years 1960-2008. The black line is the zero contour.

Figure 4.9 shows the mean barotropic streamfunction of years 1960-2008. The flow travels parallell to the contours where blue (red) colours indicate a cyclonic (anticyclonic) circulation. The strongest cyclonic circulation is found in the western part of the SPG with a maximum of –40 Sv. In chapter 5, the barotropic streamfunction response on a NAO^+ forcing relative to the NAO^n forcing will be discussed.

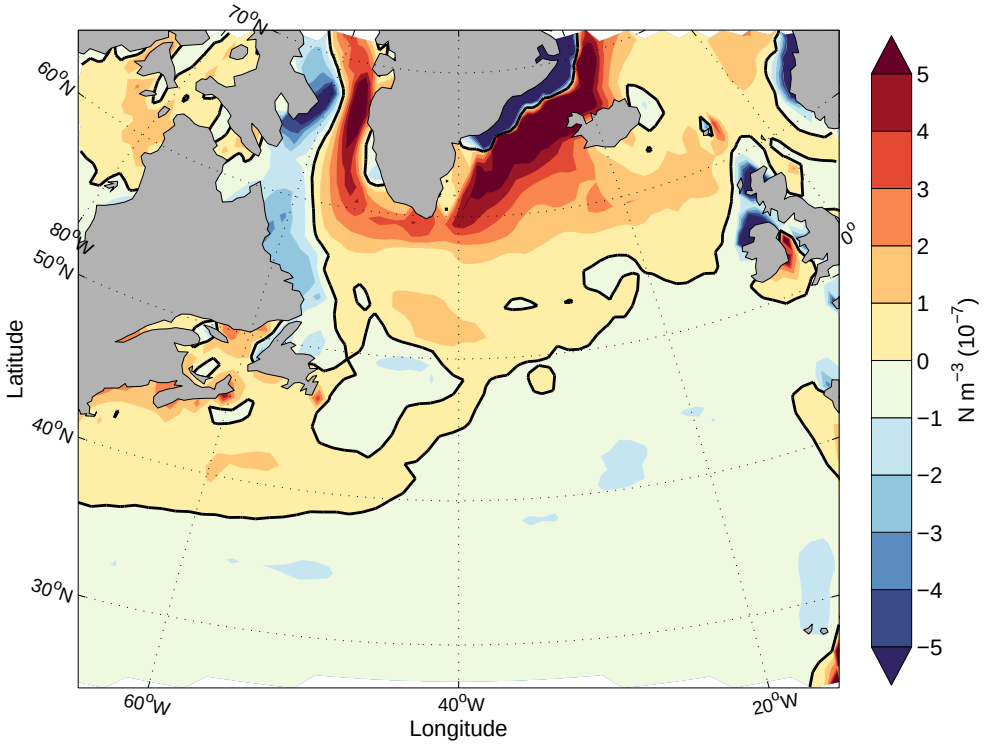

Figure 4.10: Mean wind stress curl of years 1960-2008. The black line is the zero contour.

Figure 4.10 shows the mean wind stress curl in the North Atlantic for the period 1960-2008. Blue colouring shows negative (anticyclonic) wind stress curl, which is located in the STG region stretching towards north-western Europe. The red colouring shows positive (cyclonic) wind stress curl, which occupy large parts of the SPG region and the Nordic Seas. The black line shows the location of the zero wind stress curl, which is a region of zero Ekman pumping/suction and zero Sverdrup transport, and approximately defines the boundary between the two gyres which will be discussed in chapter 5. As mentioned in section 2.3, positive wind stress curl is associated with divergent Ekman transport, while negative wind stress curl is associated with convergent Ekman transport. Thus, the mean conditions for the period 1960-2008 is Ekman suction (horizontal Ekman transport divergence) in the SPG and Ekman pumping (horizontal Ekman transport convergence) in the STG.

Figure 4.11 shows contour lines of the mean mixed layer depth in March and September, representing a typical winter and summer situation. The mixed layer depth is, in general, larger in March than in September. Deepest mixed layer depth is located in the Labrador Sea where the contour lines are monotonically increasing towards 550 m. The mixed

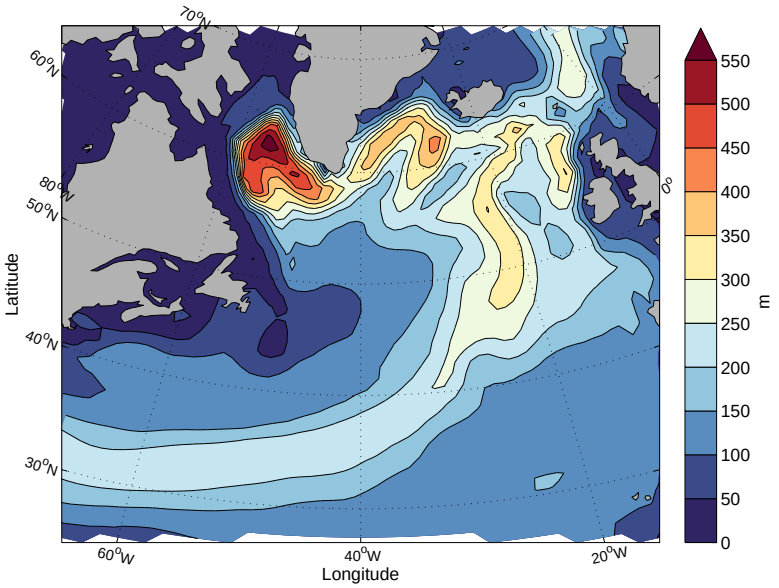

(a) March

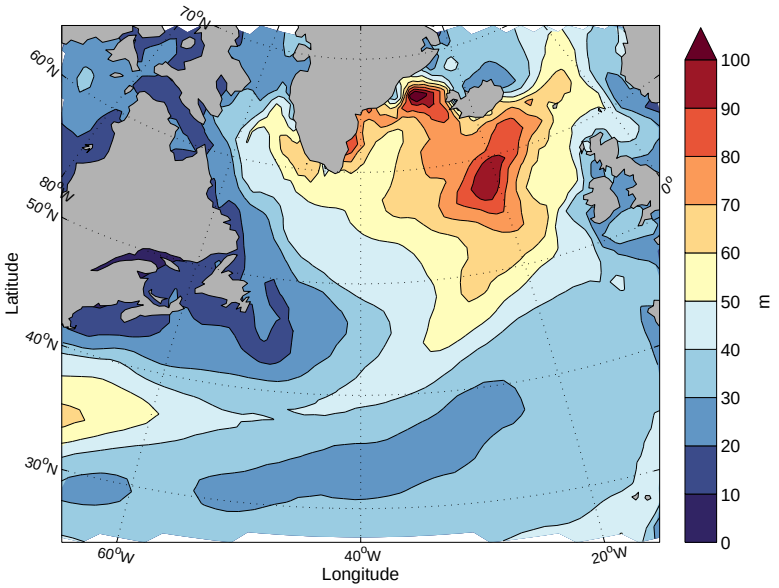

(b) September

Figure 4.11: Mean mixed layer depth in March **(a)** and September **(b)** of years 1960-2008.

layer reaches between 300 to 400 m in the Irminger Sea southeast of Greenland. This finding is different from Bentsen et al. (2004), who found that the deepest mixed layer was located in the Irminger sea, with the largest inter-annual variability in the Labrador Sea. The Bentsen et al. (2004) study is, however, based on an earlier version of the OGCM used in this study, and it is forced with older reanalysis products, so differences can be expected.

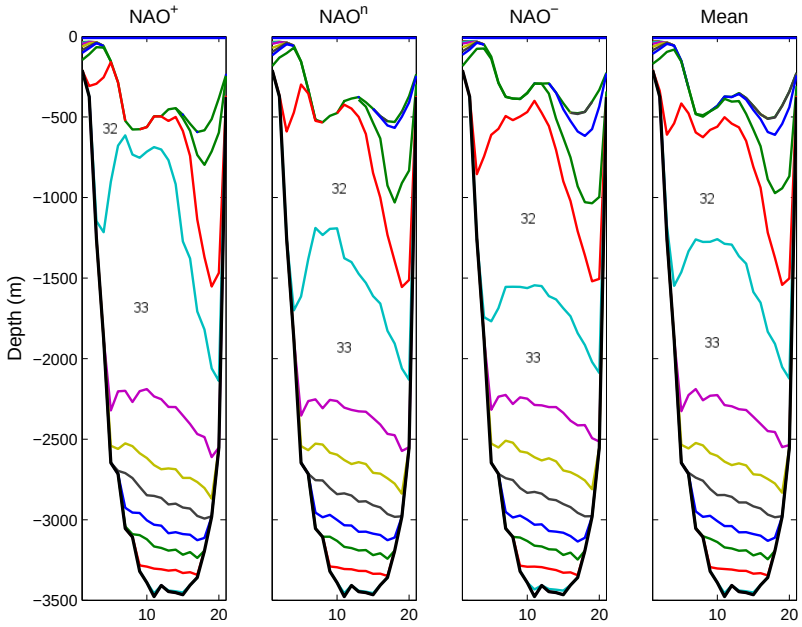

(a) ERA40

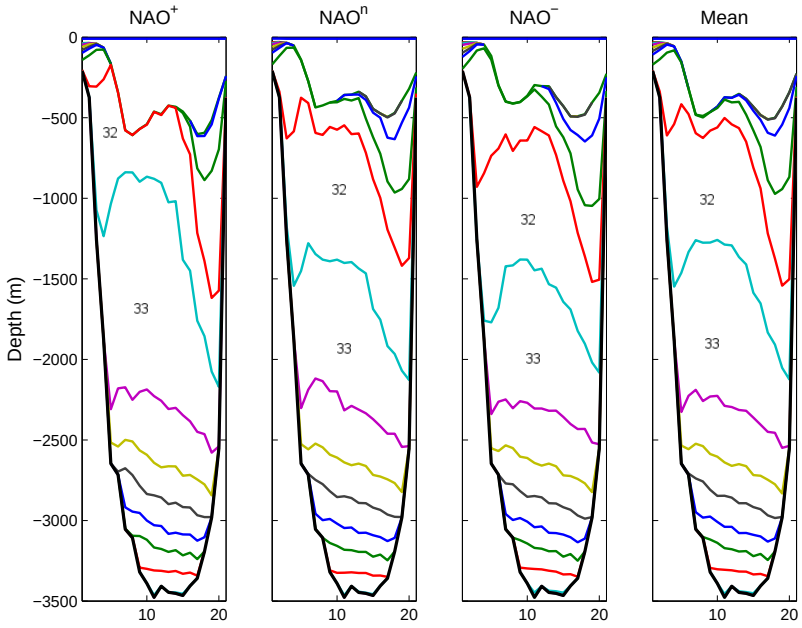

(b) NCEP-NCAR

Figure 4.12: Distribution of model layers in March from New Foundland to Greenland along the transect 59 °W,55 °N to 48.5 °W,61 °N (see black line in Fig. 4.13(a), running from West to East). Values are based on the NAO^+, NAO^n and NAO^- composites and are averaged over the years 1960-2008. **(a)** displays the ERA40 composites, while **(b)** displays the NCEP-NCAR composites.

Figure 4.12 shows the relationship between the NAO index and the vertical distribution of model layers across the Labrador Sea for the ERA40 and NCEP-NCAR composites. The thickest layers are layer number 32 and 33 which are also those layers with the

largest variability. These layers have a potential density of σ_θ = 36.789 and σ_θ = 36.843, respectively. For the positive NAO forcing, the convective mixing reaches between 2000-2500 m as indicated by variations in the thickness of model layer 33 and with only small changes in the layer distribution at greater depths. This layer dominates at intermediate depths between 1000-2000 m with a maximum thickness in the central part of the section for the NAO$^+$ forcing, which is about twice the thickness for the NAO$^-$ forcing.

The main differences between the two sets of composites are greater thickness of layer number 33 in the ERA40 NAO$^+$ composite, as well a smaller thickness in the ERA40 NAO$^-$ composite for the same layer. In Fig. 4.12(b), the NAO$^-$ composite is almost identical with the NAO^n composite.

Figure 4.13(a) shows the simulated thickness of model layer 33 in March in the northern North Atlantic Ocean for the ERA40 NAO$^+$ composite. The ERA40 version is used because it showed larger response than the NCEP-NCAR version in Fig. 4.12. Largest values are found in the Labrador Sea with a maximum value of about 1500 m near the center of the transect. Deep convection is also located in the central SPG with typicall values of 1200-1400 m.

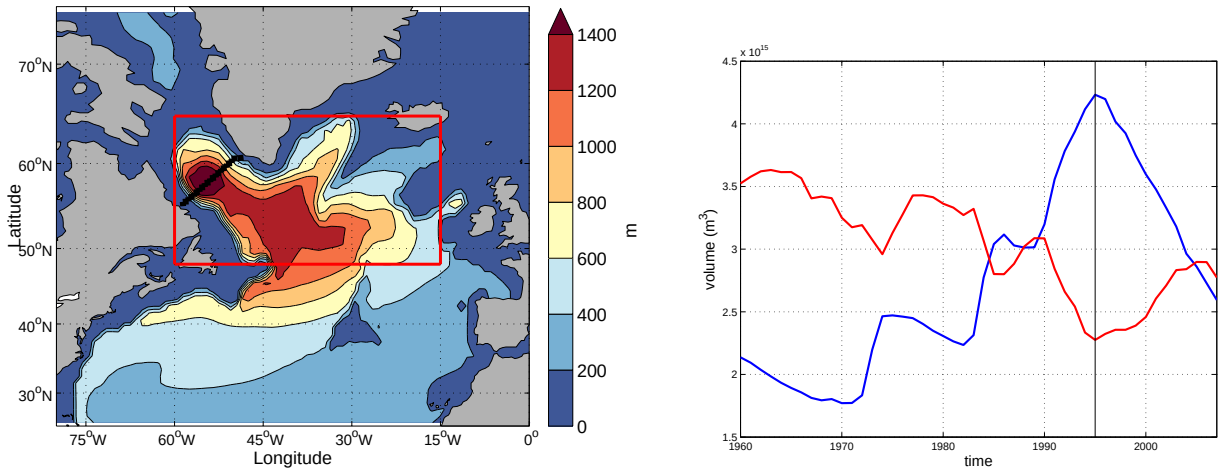

(a) Layer thickness

(b) Volume

Figure 4.13: (a) Mean layer thickness of model layer 33 in March for the ERA40 based NAO$^+$ composite. The red rectangle is used as the definition of the SPG region confined to between 60 °W-15 °W and 48 °N-65 °N. **(b)** Volume of model layer 32 (red line) and 33 (blue line) averaged annually over the SPG region between 1960-2008. Grid cells where model layer 33 is absent are removed before averaging. The black vertical line indicates the year 1995.

The volume time series of the thickness of layer 32 and 33 in the SPG region, are shown

in Figure 4.13(b). There are small year-to-year variations, but with distinct variations on inter-annual to decadal time scales. The minimum value is found around 1970 with a volume of about 1.7×10^6 km^3, which is followed by a long-term positive trend. The maximum value is found in 1995 (black vertical line) with a volume of around 4.4×10^6 km^3, before it decreases with a fairly constant rate of about 1.3×10^5 km^3 per year. The correlation coefficient between the thickness of layer 32 and 33 is –0.92, indicating that 85% of the variance in the time series are inversely related.

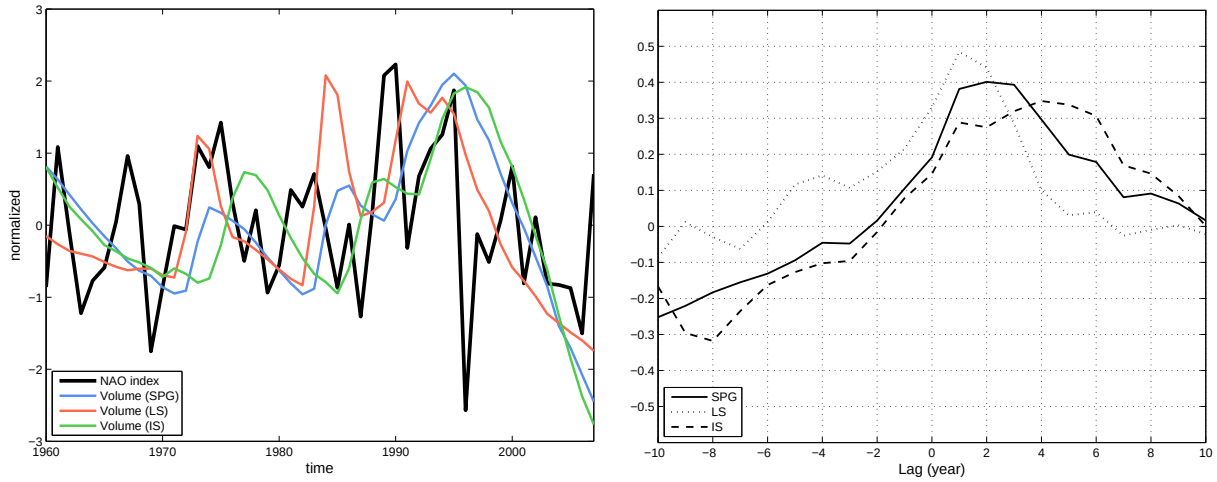

(a) Volume **(b)** Cross-correlation

Figure 4.14: (a) shows the NAO index (black line) compared with the volume of model layer 33 averaged over the SPG (blue), LS (red) and IS (green). **(b)** shows the cross-correlation between the NAO index and corresponding volume indices. Positive lag means that the NAO index lead the corresponding volume index.

Figure 4.14 shows the NAO index and volume of model layer 33 averaged over the SPG region, the Labrador Sea (LS) and the Irminger Sea (IS). The volume from the SPG region is the same as shown in Figure 4.13(b). The LS volume is averaged over the region 59 °W-50 °W and 56 °N-62 °N, whereas the IS volume is averaged over the region 42 °W-30 °W and 55 °N-64 °N. As discussed earlier, the LS is a place where deep convective mixing takes place. The modelling results from Bentsen et al. (2004) found that the IS is also a region of deep convective mixing, which is supported by Pickart et al. (2003) based on tracer observations and similarities between the atmopsheric conditions over the LS and IS. However, Figure 4.13(a) indicate that the IS is less important when it comes to deep convetion since the IS shows relative small layer thickness of model layer 33 compared to the LS and central SPG. Figure 4.14(b) shows the cross-correlation between the annual

mean NAO index and the three volume indices. The LS is the region that most instantly respond to the NAO forcing with a peak correlation lag of 1 year. The IS lag the NAO index by 2-6 years, while the SPG region, which includes both the LS and IS lag the NAO index 1-3 years. The cross-correlations at these time lags were all above the 95% significance lines (not shown).

4.4 SPG indices and AMOC

Figure 4.15 shows the barotropic streamfunction averaged over the SPG region. Strong gyre circulation corresponds to large negative values (note that the y-axis is reversed). Figure 4.15(b) shows SSH anomalies, which is another indicator of the strength of the SPG. Strong gyre circulation corresponds to low SSH (oriented upwards in the figure). The model simulates rather realistically the observed (Cunningham et al., 2007) (red line) decrease in SSH between 1995 and 2008, although the observed data show two peaks in 2000 and 2005 which are absent from the model. Figures 4.15(c) and 4.15(d) shows the maximum strength of the AMOC at 41°N and 26.5°N, respectively. At 26.5°N, observation-based data (Church et al., 2011) is indicated by the red line running from 2004 to 2008. It shows that the strength of the simulated AMOC is reasonable, although a large increase observed in 2007 is missing in the model. An extended integration is needed to check whether the simulated AMOC increases in e.g. 2008.

Figure 4.16 shows that the SSH index leads the barotropic streamfunction (BSF) index with a peak correlation of 0.73 at one year, and the AMOC at 41°N with a peak correlation of –0.57 at one year. Correlation is low between the AMOC at 41°N and 26.5°N where maximum correlation is found at minus 1 year and plus 8 years. All peak correlations were above the 95% significance lines (not shown).

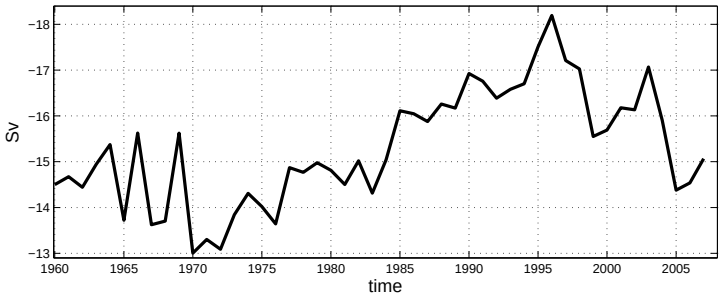

(a) Barotropic streamfunction

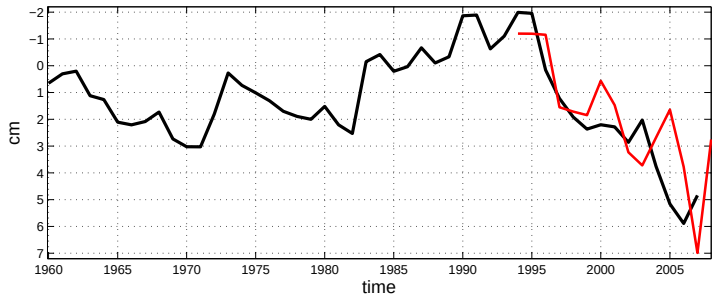

(b) SSH

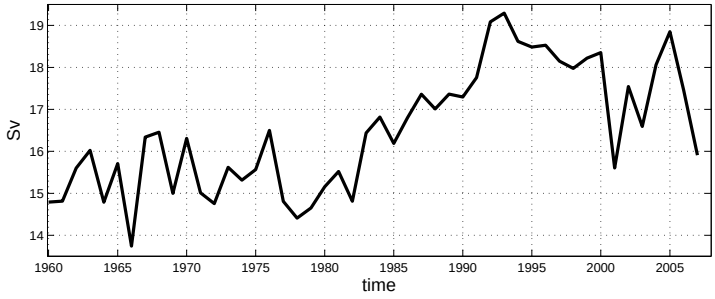

(c) AMOC at 41° N

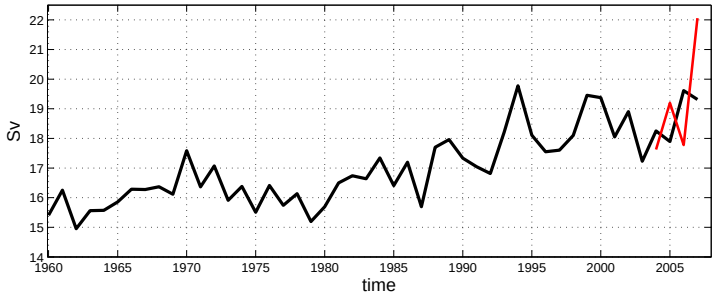

(d) AMOC at 26.5° N

Figure 4.15: **(a)** Annual barotropic streamfunction averaged over the SPG region (60 °W-15 °W, 48 °N-65 °N). **(b)** Annual SSH anomalies with respect to the 1993-1999 mean averaged over the SPG region. The red line is the corresponding sea level data obtained from http://www.cmar.csiro.au/sealevel/sl_data_cmar.html, which is a combination of data from TOPEX/Poseidon, Jason-1 and Jason-2/OSTM. **(c)** and **(d)** is the annual mean of monthly maximum strength of the AMOC at 41°N and 26.5°N, respectively. The red line is the observation-based maximum AMOC at 26.5°N based on 12-hourly, 10 day low passed filtered data obtained from http://www.noc.soton.ac.uk/rapidmoc/. The data is averaged annually as the model data. The y-axis in **(a)** and **(b)** are reversed and the annual averages consists of monthly values going from July to June, where January indicate the year number.

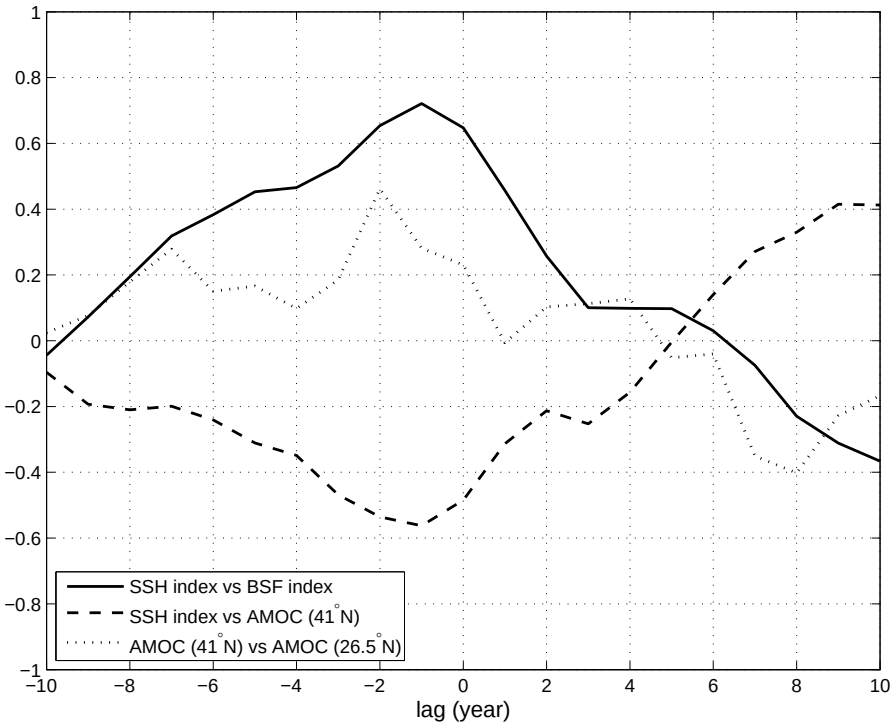

Figure 4.16: Cross-correleation between SPG indices, the SSH index and AMOC at 41°N and the AMOC at 41°N and 26.5°N. Negative lag means that the first index leads the second.

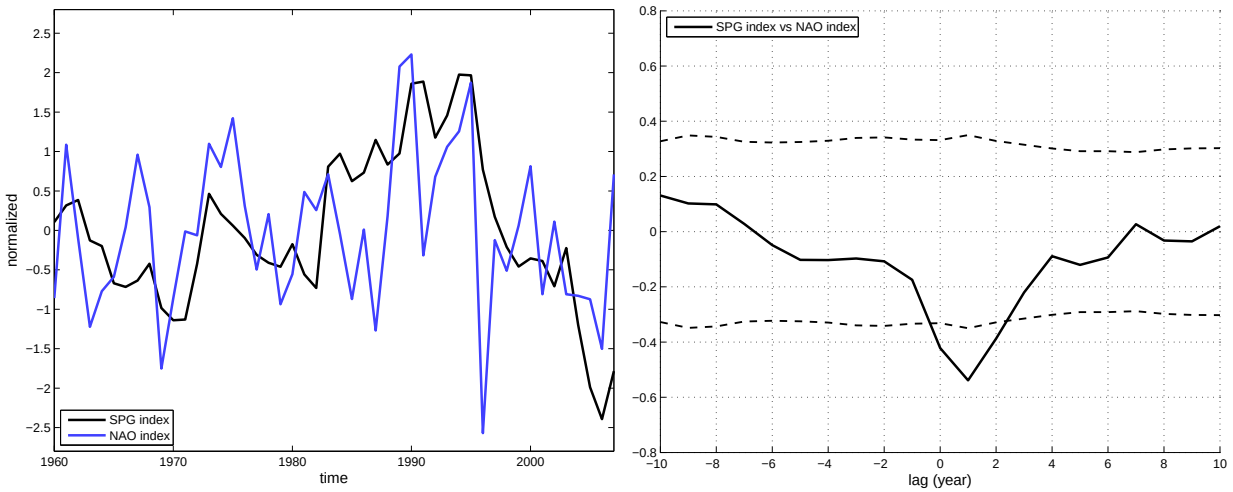

Figure 4.17: **(a)** Normalized SSH-based SPG index and NAO index where the SPG index has been reversed. **(b)** Cross-correleation between the SSH-based SPG index and the NAO index. Positive lag means that the NAO index leads the SPG index. The dashed lines indicate the 95% significance lines. In the estimation of the significance lines, the number of degrees of freedom are adjusted at each lag, where auto-correlation has been accounted for.

Cross-correlation between the SSH-based SPG index and the NAO index is dislayed in Figure 4.17. The cross-correlation is significant at the 95% confidence level between 0 and 2 years positive lag, with a peak correlation at 1 year lag of –0.54. This means that 29% of the variance in the SPG index is due to variations in the NAO index one year earlier. In the next section, more correlation coefficients will be presented between the SPG indices and indices from EOF analyzes. The SSH index is choosen as the master index since it correlates better with the other indices, which is shown in Table 4.2.

4.5 EOF analysis

A SVD is used to extract the leading mode of variability in Figures 4.18 to 4.24. Some time series are reversed to match the SSH-based SPG index (or NAO index). Multiplying the values from the regression fields somewhere in the domain with the values of the normalized PC1 at a specific time gives the associated anomaly at that location and time. Thus, the EOF analysis reveal the leading spatial and temporal anomalies of the data sets that are analyzed.

Figure 4.18(a) shows the EOF analyzes based on altimetry data in the left panel and simulated SSH in the right panel from the period 1993-2008. The corresponding PC's are displayed in Fig. 4.18(b), shown as red and blue lines, respectively. The correlation coefficient between the SPG index and the SSH-based PC is 0.97, displayed in table 4.1, while the correlation between the altimetry-based PC1 and SPG index is not significant different from zero at the 90% confidence level on this time scale. However, both the altimetry and SSH-EOF patterns show a similar dipolar pattern as the SSH for the NAO^+ forcing in Fig. 4.7(a), with a slight eastward shift of the negative SSH anomaly pattern in the SPG.

Figure 4.19 shows the EOF analyzes of the same variables, but based on the winter mean from the period 1993-2008. As can be seen in the EOF patterns, the dipolar pattern is shifted even further to the east than for the deseasonalized versions. These patterns are more similar to the NAO pattern in Figs. 4.3(b) and 4.5 than the SSH in Fig. 4.7(a). Thus, the normalized PC's are compared to the NAO index, where both correlations are significant different from zero at the 90% confidence level.

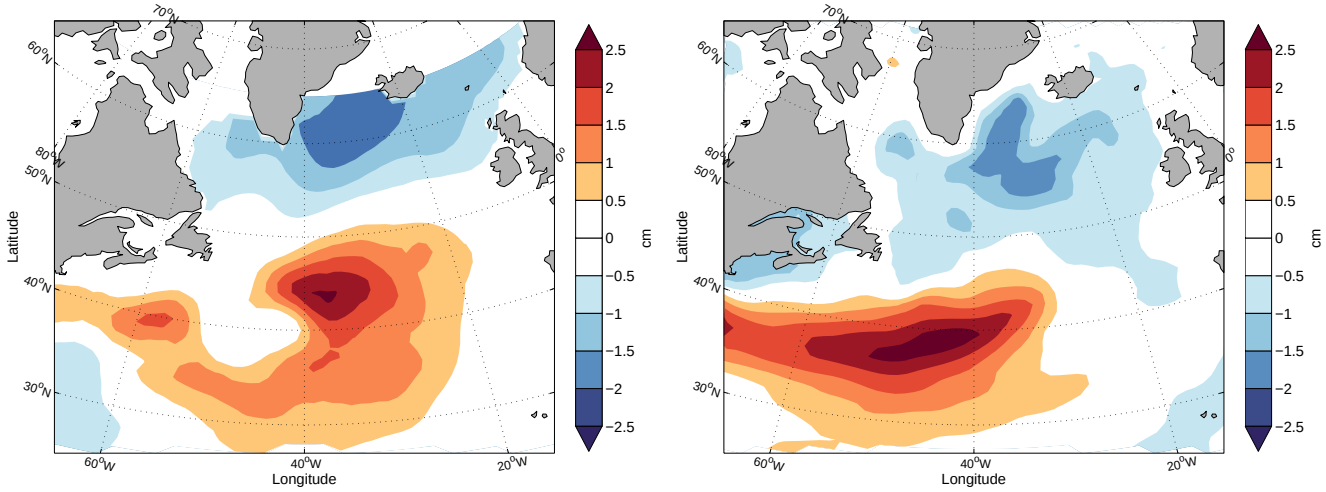

(a) Altimetry and SSH

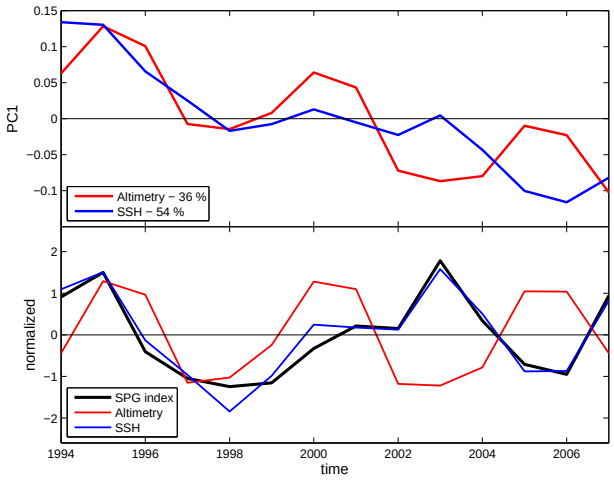

(b) PC1

Figure 4.18: **(a)** The normalized PC's from the EOF analysis of monthly altimetry data (left panel) and simulated SSH (right panel) from the North Atlantic region 75 °W-15 °W and 30 °N-65 °N, regressed on the corresponding data sets. The altimetry data is obtained from http://www.cmar.csiro.au/sealevel/sl_data_cmar.html. Both data sets are from the period 1993-2008, where the seasonal trends are removed with a running mean of 12 months before the SVD is executed. **(b)** PC1 and variance explained by the PC1 is displayed in the upper panel. The lower panel shows the normalized PC's compared with the normalized SPG index. The time series are from the period 1994-2008 because the first half of the year in the PC's are removed.

Figures 4.20 to 4.24 shows EOF analyzes based on SSH, ocean temperature (OT) and ocean salinity (OS) averaged over the upper 700 m, heat flux (HF) and wind stress curl (WSC) for the period 1960-2008. The regression fields of the normalized PC1 and the corresponding variable is displayed in the upper left figure, while the amount of variance

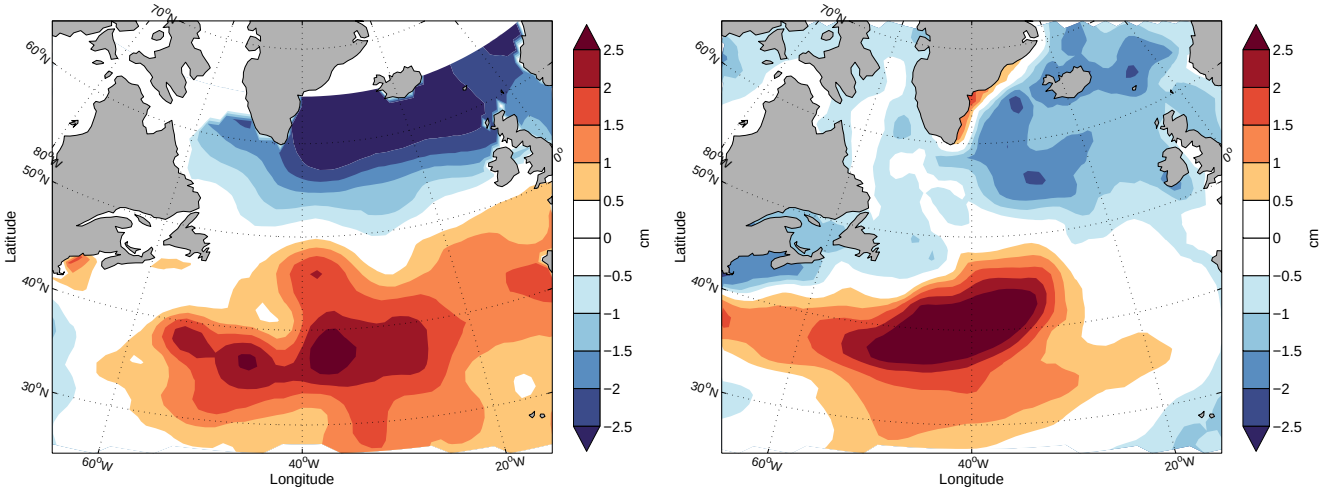

(a) Altimetry and SSH

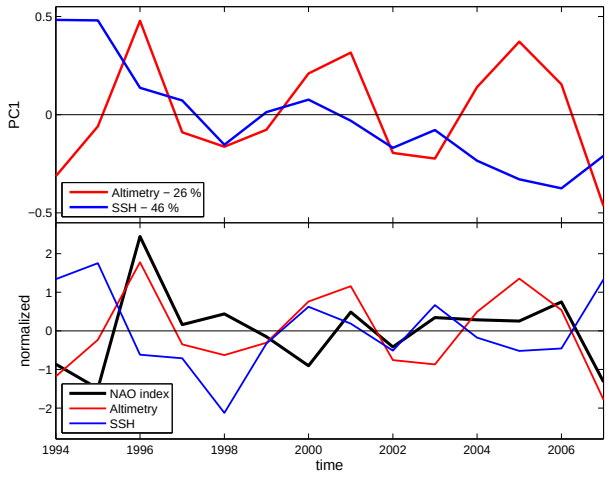

(b) PC1

Figure 4.19: Same as Fig. 4.18, but EOF analysis based on data averaged over winter months (December-March) instead of deseasonalized data. The PC's are compared to the normalized NAO index from 1994-2008.

explained by the PC1 of the corresponding data set is displayed in the upper left corner of the time series panels. The SSH, ocean temperature and heat flux all show an anomaly pattern with negative values in the SPG and positive values in the STG. The ocean salinity does also show a dipolar pattern, with opposite sign. The heat flux consists of the sensible, latent, shortwave and longwave components, as well the advective heat flux, where negative anomalies indicate heat loss from the ocean. The wind stress curl in Fig. 4.24 indicates a negative anomaly in the SPG below a positive anomaly close to Iceland, where positive curl anomalies corresponds to a cyclonic circulation anomaly.

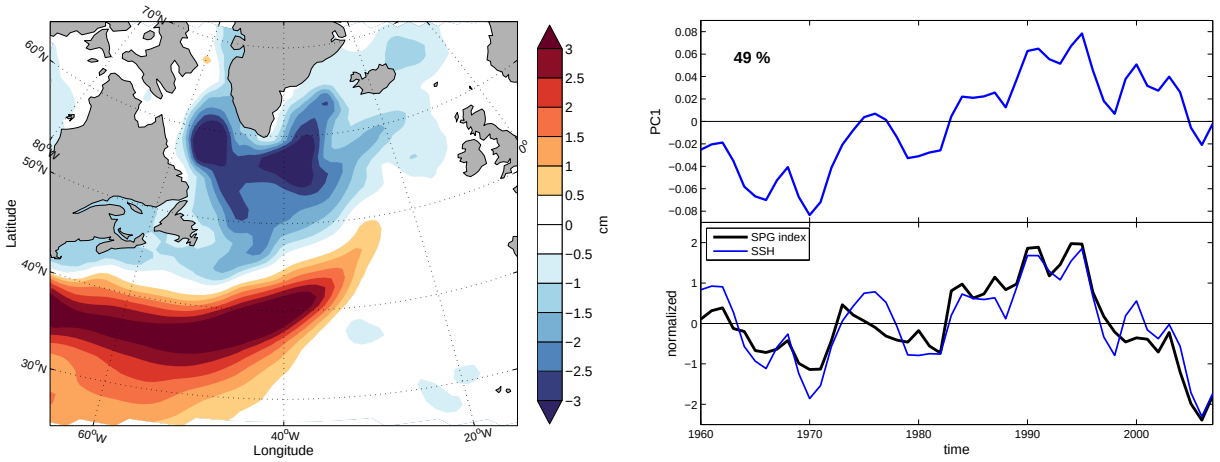

(a) SSH **(b)** PC1

Figure 4.20: (a) Monthly SSH regressed on the normalized PC1. The seasonal trend is removed with a running mean of 12 months before the SVD analysis is executed. The EOF analysis is based on data from the North Atlantic area 75 °W-15 °W and 30 °N-65 °N. **(b)** The lower panel shows the normalized PC1 compared with the normalized SPG index. The variance explained by the PC1 is displayed in the upper panel.

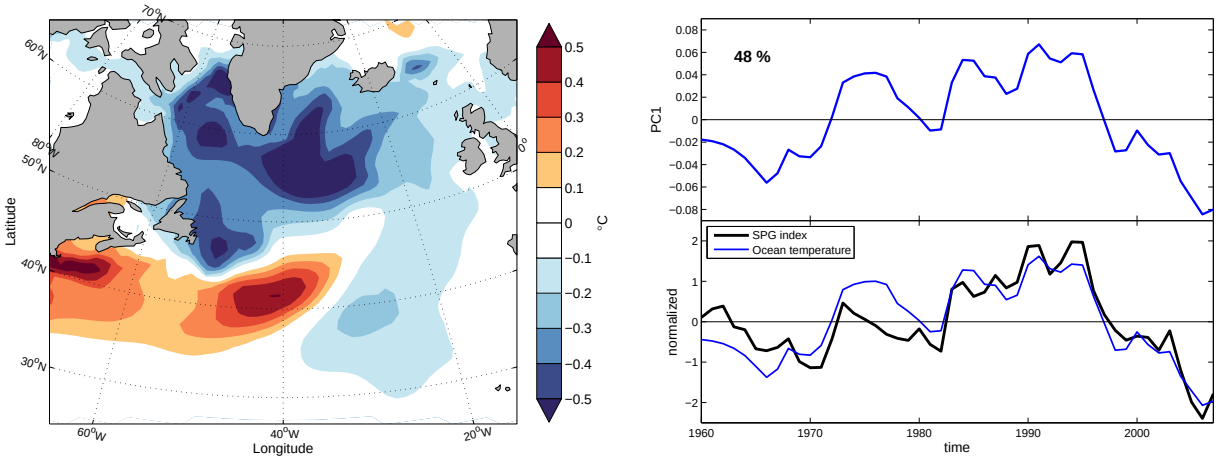

(a) Ocean temperature (upper 700 m) **(b)** PC1

Figure 4.21: Same as Figure 4.20, but for ocean temperature averaged over the upper 700 m.

Table 4.2 shows correlation coefficients between the indices from the EOF analyzes and SPG indices. All variables correlated with the SSH index are significant different from zero at the 90% confidence level. As expected, the correlation between the PC1 and SPG index in Figure 4.20 is high, since both are based on the SSH. Ocean temperature in Figure 4.21 shows higher correlation than the ocean salinity in Figure 4.22, which is consistent with the result in Figure 4.6 where temperature is the dominant contribution

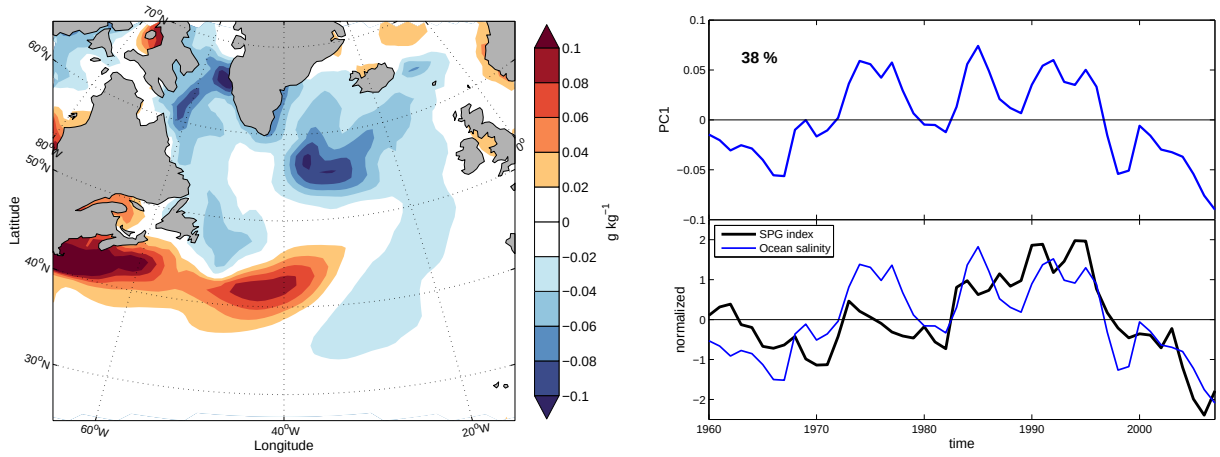

(a) Ocean salinity (upper 700 m) **(b)** PC1

Figure 4.22: Same as Figure 4.20, but for ocean salinity averaged over the upper 700 m.

to the SSH. The table also shows that the heat flux leads the SSH index and the other indices by one year, and is the only index that shows a higher explained variance for the winter average than the annual average (39% and 28%, respectively), except the WSC which also shows a small percentage higher for the winter average (38% and 36%, respectively).

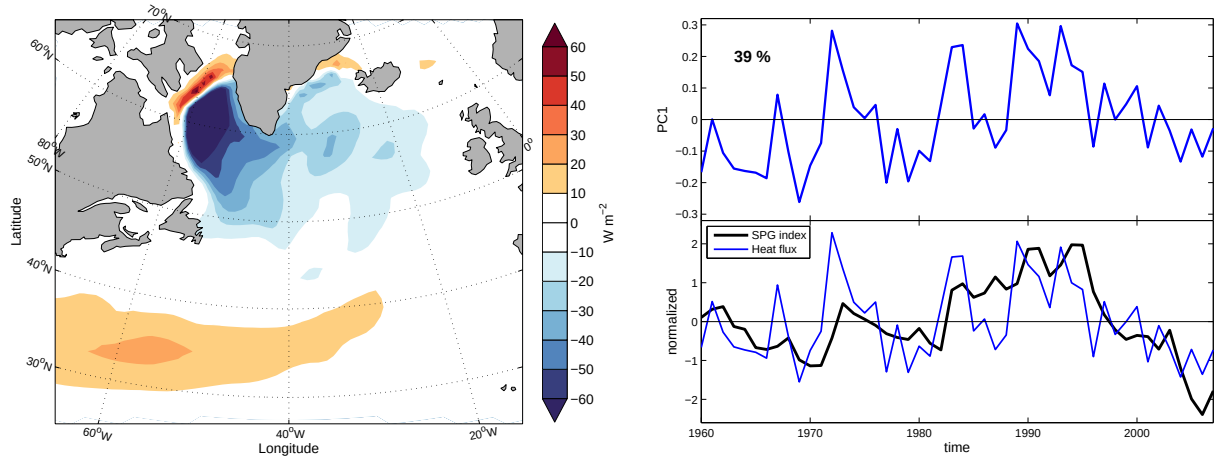

(a) Heat flux **(b)** PC1

Figure 4.23: Same as Figure 4.20, but for heat flux averaged over winter months between December and March instead of deseaonalized data.

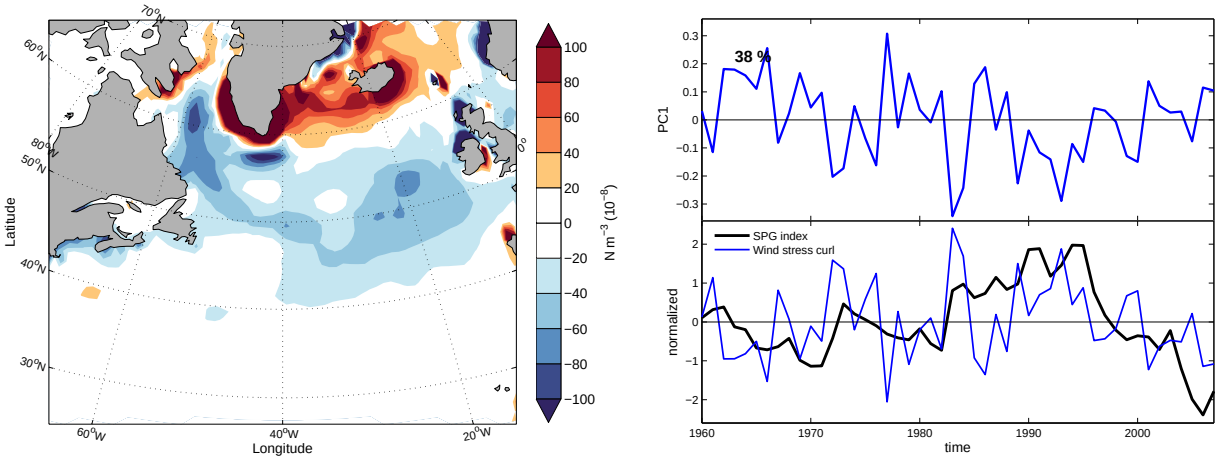

(a) Wind stress curl **(b)** PC1

Figure 4.24: Same as Figure 4.20, but for wind stress curl averaged over winter months between December and March instead of deseaonalized data.

Table 4.1: Lagged peak correlations (r), and varianced explained (r^2) between the SPG index from 1994-2008 and PC's from Fig. 4.18 in **(a)**, and from Fig. 4.19 in **(b)**. Positive lag means that the variables lead the SPG index. The percent numbers are the variance explained by the corresponding PC1. The correlatios in bold are significant above the 90% confidence level using a double sided t-test. In the estimation of the t-distribution, the number of degrees of freedom is adjusted due to autocorrelation.

(a) July-June

	Altimetry (36%)	SSH (54%)
SPG index		
r	-0.36 (5 yr)	**0.97** (0 yr)
r^2 (%)	13	94

(b) Winter

	Altimetry (26%)	SSH (46%)
NAO index		
r	**-0.63** (0 yr)	**-0.64** (0 yr)
r^2 (%)	40	41

Table 4.2: Lagged peak correlations (r), and varianced explained (r^2) between the PC1 indices and the SPG indices based on SSH and barotropic streamfunction. **(a)** is based on the normalized PC's of the annual data running from July-June, while **(b)** is based on the winter mean data (December-March). Positive lag means that the variables lead the corresponding SPG index. The percent numbers are the variance explained by the corresponding PC1. The correlatios in bold are significant above the 90% confidence level using a double sided t-test. In the estimation of the t-distribution, the number of degrees of freedom is adjusted due to autocorrelation.

(a) July-June

	SSH (49%)	OT (48%)	OS (38%)	HF (28%)	WSC (36%)
SSH index					
r	**0.90** (0 yr)	**0.87** (0 yr)	**-0.72** (0 yr)	**0.74** (1 yr)	**0.4** (0 yr)
r^2 (%)	81	76	52	55	16
BSF index					
r	**0.69** (1 yr)	0.51 (1 yr)	-0.37 (1 yr)	**0.49** (2 yr)	0.25 (4 yr)
r^2 (%)	47	26	14	24	6

(b) Winter

	SSH (45%)	OT (44%)	OS (32%)	HF (39%)	WSC (38%)
SSH index					
r	**0.86** (0 yr)	**0.87** (0 yr)	**-0.69** (0 yr)	**0.69** (1 yr)	**0.43** (0 yr)
r^2 (%)	74	76	49	48	18
BSF index					
r	**0.67** (1 yr)	0.51 (1 yr)	-0.36 (5 yr)	**0.43** (2 yr)	**0.26** (4 yr)
r^2 (%)	45	32	13	19	7

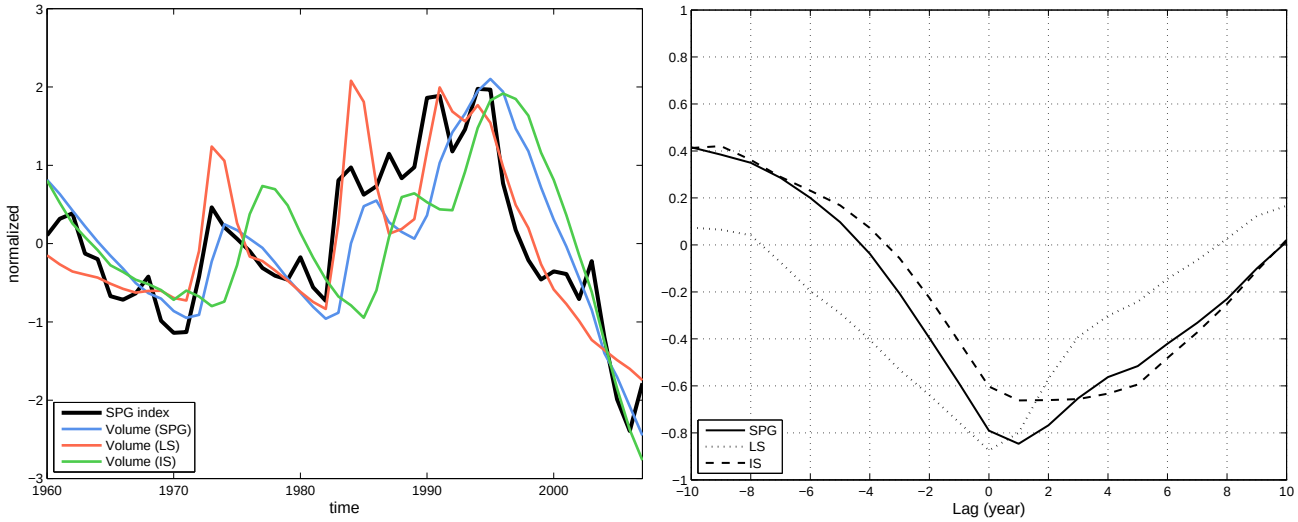

(a) SPG index

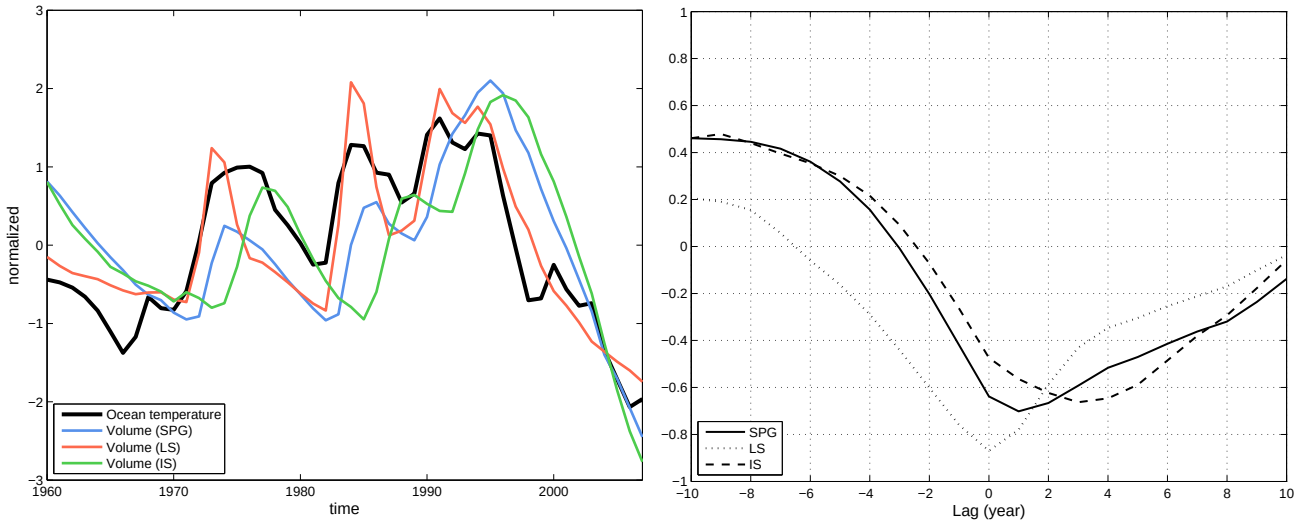

(b) Ocean temperature

Figure 4.25: Left panels show the SPG index **(a)** and PC1 of ocean temperature **(b)** compared with the normalized volume of model layer 33 averaged over the SPG region, LS and IS for years 1960-2008. Right panels show cross-correlation between volume indices and the **(a)** SPG index and **(b)** ocean temperature. Positive lag means that the corresponding index lead the volume indices.

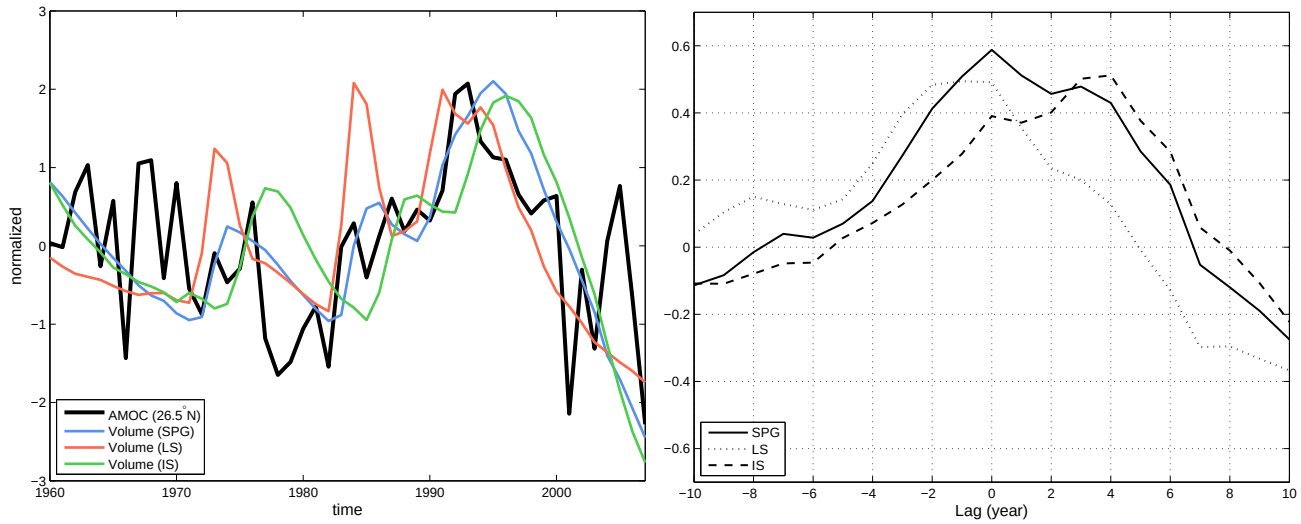

(a) AMOC at 41 ° N

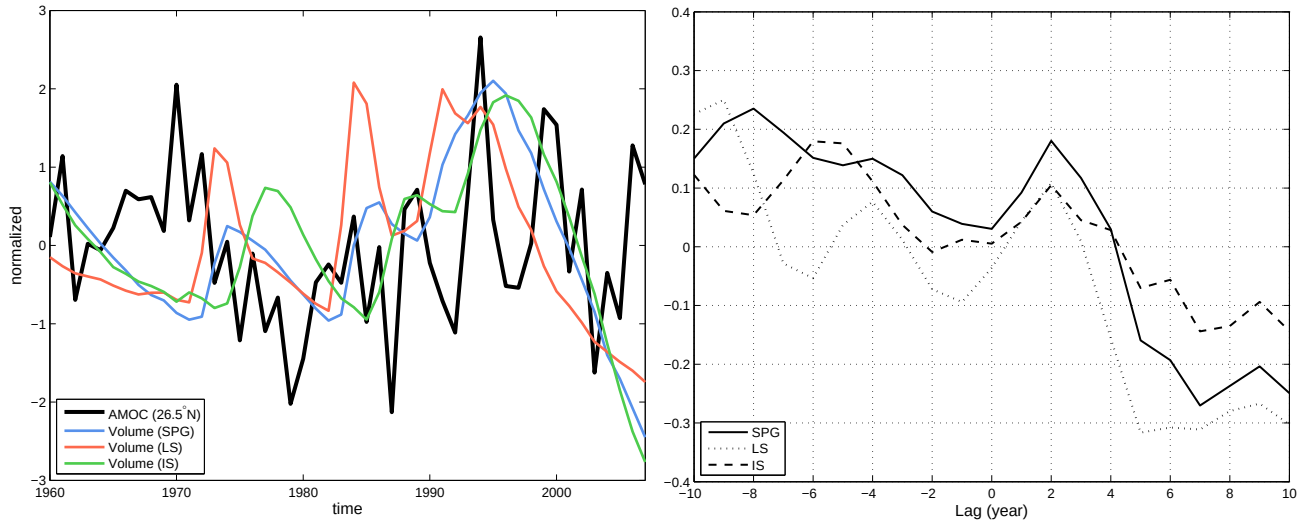

(b) AMOC at 26.5 ° N

Figure 4.26: Left panels show the AMOC at 41 °N **(a)** and AMOC at 26.5 °N **(b)** compared with the normalized volume of model layer 33 averaged over the SPG region, LS and IS for years 1960-2008. Right panels show cross-correlation between volume indices and the **(a)** AMOC at 41 °N and **(b)** AMOC at 26.5 °N. Positive lag means that the corresponding index lead the volume indices.

Figure 4.25(a) shows the normalized volume of model layer 33 over the SPG region, as well the LS and IS which are part of SPG region. The volume indices are compared with the SSH-based SPG index where the SPG index responds instantaneous with the LS volume, while the volume from the SPG region and IS lags the SPG index by 1 and 0-5 years, respectively. The PC1 of the ocean temperature in Fig. 4.25(b) shows a similar result which is expected since the ocean temperature and SPG index have a high peak correlation at zero lag (Table 4.2). All peak correlations in Figs. 4.25(a) and 4.25(b) were above the 95% significance line (not shown).

Figure 4.26 shows the volume from the different convection sites compared with the AMOC at 41°N and at 26.5°N. The AMOC at 41°N goes from a positive lag with the IS at 2-5 years towards a negative lag in the LS where the LS volume lead the AMOC by 0-2 years. The peak correlations between the volume indices and the AMOC at 41°N were all above the 95% significance line (not shown). At 26.5°N, however, the 95% significance lines were above the corresponding cross-correlation at any lag for all three volume indices. Thus, there is no significant relation between the AMOC 26.5°N and the volume indices at the 95% confidence level.

Chapter 5

Discussion

5.1 Ocean temperature and salinity in the upper 2000 m

In section 4.3, the ocean temperature and salinity response on the NAO^+ and NAO^- forcings relative to the neutral NAO state were examined. The upper 400 m was choosen because this depth interval encompass the seasonally ventilated SPG and STG water masses. Here we also discuss the response from the upper 2000 m (not shown). The ocean temperature anomalies were in good agreement with the pattern shown for the upper 400 m, but with slightly weaker amplitudes. The ocean salinity, however, shows much weaker amplitudes and no consistency with the pattern shown for the upper 400 m. Furthermore, no consistency is found between the NCEP-NCAR and ERA40 based NAO composites for the deep ocean. This suggests that the surface forcing do not directly influence the deep waters, and/or that the leading time scale for variability in the deep ocean is not explicitly set by surface processes.

5.2 Mechanisms driving the NAC

The zero contour line of the mean wind stress curl of years 1960-2008 defines the mean boundary between the divergent Ekman transport in the SPG and convergent Ekman transport in the STG. It also defines the region where the depth-integrated meridional transport is zero. Along this boundary there will be, in general, no vertical velocities

due to the vanishing divergence. Thus, the boundary will act as a guide for the NAC, keeping the water at the surface until it eventually cools at higher, northern latitudes.

The SSH depends on the steric effect from the thermal and haline contributions, as well the wind stress curl forced convergence or divergence of water masses. Figure 5.1(a) shows the mean zero contour line of the wind stress curl superimposed on the mean SSH of years 1960-2008. Geostrophic balance implies that the strongest ocean currents will be located where the SSH gradients are largest. The SSH gradient is shown as contours in Figure 5.1(b), with a band of large gradients extending along the boundary between the SPG and STG. The rather close agreement between the SSH gradient and the zero wind stress curl west of 40 °W is likely a result of the near correspondence between strong persistant advection of warm sub-tropical waters and the upper stratification of the water column. Further east, weaker vertical stratification implies that the SSH is more influenced by hydrography and dynamics of the deeper waters.

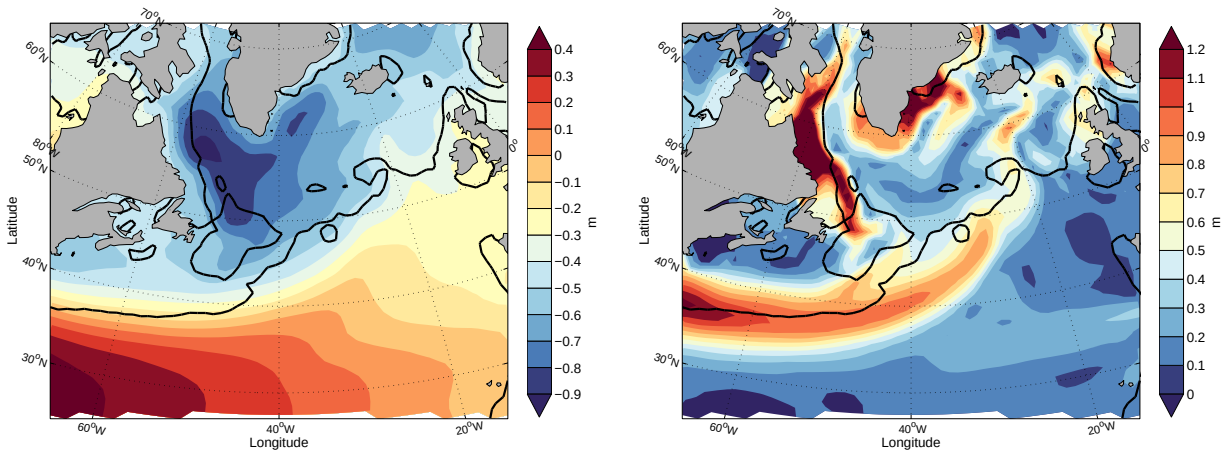

(a) SSH **(b)** SSH gradient

Figure 5.1: **(a)** Mean SSH of years 1960-2008 shown as coloured contours. **(b)** Gradient of mean SSH derived from **(a)**. The black line is the mean zero contour line for the wind stress curl of years 1960-2008.

5.3 Relation between SSH and barotropic streamfunction

The barotropic streamfunction represents the average flow of the water column. For a weakly stratified ocean, the barotropic streamfunction and SSH show a close resemblance (Marshall and Plumb, 2008, pp. 217-218). This is the case in the weakly stratified

SPG, see Figs. 4.9 and 5.1(a). Cross-correlation has also revealed that variations in the SSH are highly related to variations in the barotropic streamfunctcon (peak correlation of 0.73), where the SSH-based SPG index leads the barotropic streamfunction index by one year. This suggests that a common mechanism drives the variations with a lag between the corresponding response.

In section 4.3, we showed that the SSH is determined by the atmospheric forcing, with ocean temperature in the upper 400 m as the dominant contributor. This is supported by correlations between the SSH-based SPG index and leading PC of temperature and salinity, where temperature showed highest correlation (see table 4.2). We also demonstrated that the layer thickness of model layer 33 increased during NAO^+ forcing as a result of convective mixing. Figure 5.2 shows the response of the barotropic streamfunction to a NAO^+ forcing relative to the neutral state. The NAO^+ forcing increases the cyclonic circulation in the SPG with a maximum anomaly in the LS of more than 5 Sv. Elsewhere, the anticyclonic circulation is strengthened along the NAC. The ERA40 anomalies also show a decrease in the anticyclonic circulation in the STG. In the SPG, the pattern resembles the SSH response from NAO^+ forcing relative to the neutral state, indicating that a common mechanism driving the variations in the SSH and barotropic streamfunction is the atmospheric forcing represented by the NAO index. Since the buoyancy of the upper ocean acts to accumulate the atmospheric forcing over time, the intermediate layers will be influenced by the atmospheric forcing after the upper ocean

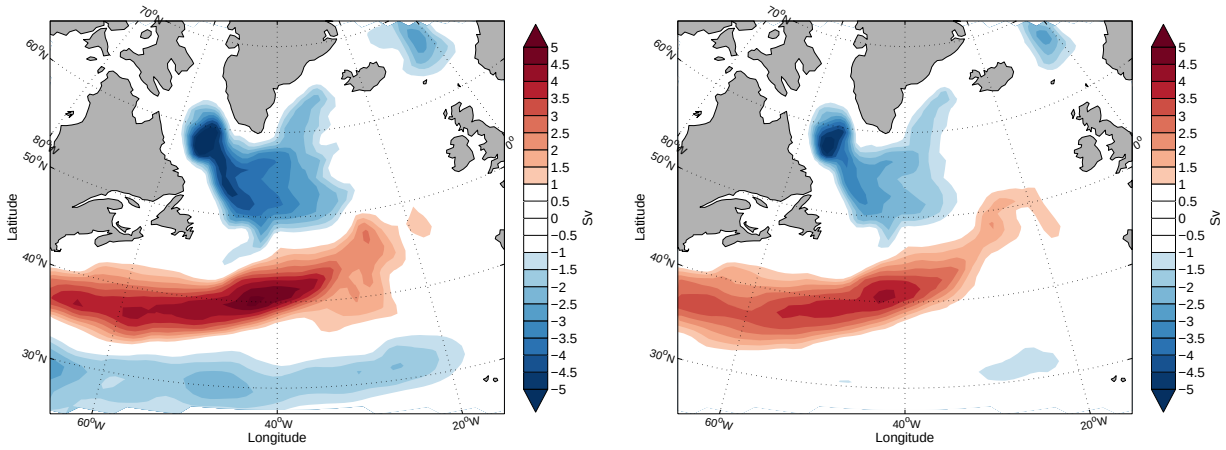

(a) ERA40 **(b)** NCEP-NCAR

Figure 5.2: Difference in barotropic streamfunction between years with NAO^+ and NAO^n forcing of the ERA40 based NAO index (right panel) and NCEP-NCAR based NAO index (left panel).

is affected. This explains the delay of the barotropic streamfunction to the SSH. However, one should be careful of excluding other mechanisms, considering that the NAO index "only" explained 29% of the variance in the SSH-based SPG index (see section 4.4).

5.4 Idealised model using Margules relation

If we consider the LS as a closed, circular basin, we can set up an idealised model as shown in Fig. 5.3. With the assumption that the surface elevation is bell-shaped, it can be expressed as

$$\eta_1 = h_1 + h_2 - \eta_1^* \exp(-x^2/L^2)\,. \tag{5.1}$$

Here h_1 and h_2 are as in Fig. 2.3, η_1^* is the maximum surface elevation and L is a horizontal length scale. The geostropic flow in the upper ocean follows from eq. (2.12). Substituting eq. (5.1) and noting that h_1 and h_2 are constant, gives

$$v_{g1} = 2\,\frac{g}{f}\,\frac{\eta_1^*\,x}{L^2}\exp\left(-\frac{x^2}{L^2}\right). \tag{5.2}$$

The geostropic flow vanishes in the center (x=0) and at the periphery (large x) of the gyre, as expected. The transect through the LS in Fig. 4.12 is about 900 km long. The bell-shaped surface elevation and variations in the sub-surface isopycnals do not fully extend to the periphery of the transect (see Fig. 4.13), so we may set $L = 300$ km. A typical difference in the SSH across the LS is 20 cm (see Fig. 4.2(a)). At $x = 150$ km, this gives a geostrophic speed of

$$v_{g1}(x = 150\text{ km}) \approx 0.04\text{ m s}^{-1}\,. \tag{5.3}$$

Margules relation (see eq. (2.15)) can be used to estimate the simulated thermal wind $v_{g1} - v_{g2}$ contribution to, for instance, NAO$^+$ composites compared to the climatological mean state. From the NAO+ panels in Fig. 4.12, the fall of the interface between layer 32 and 33 is about 1000 m (for the northern half of the gyre). The corresponding fall for the climatological mean is around 500 m. Thus, NAO$^+$ forcing increases the isopycnic slope with about 500 m compared with the climatological state. The sloping isopycnals occurs over a distance of about 300 km. Furthermore, the density difference between layer 32 and 33 is about 0.05 kg m^{-3}. Writing $\gamma = \Delta z/\Delta x$, these numbers give

$$\frac{\partial \eta_2}{\partial x} \approx \frac{-500\text{ m}}{300\cdot 10^3\text{ m}} = -1.7\cdot 10^{-3} \quad \text{and} \quad g' \approx 9.8\text{ m s}^{-2}\frac{0.05\text{ kg m}^{-3}}{1036\text{ kg m}^{-3}} \approx 4.7\cdot 10^{-4}\text{ m s}^{-2}$$

Therefore, eq. (2.15) becomes

$$v_{g1} - v_{g2} \approx 0.006 \text{ m s}^{-1}.$$

As an estimate of the change in the surface circulation, one can assume an additional contribution to v_{g1} of about 0.6 cm s^{-1}. The near-surface circulation speed may therefore increase by around 15 % compared to the climatological mean of about 4 cm s^{-1} (the latter from 5.3). This very rough estimate is consistent with an increase in the barotropic stream function of about 5 Sv for the NAO$^+$ versus the NAO^n composite (see Fig. 5.2), relative to a climatological mean value of the barotropic stream function of 30-35 Sv (see Fig. 4.9).

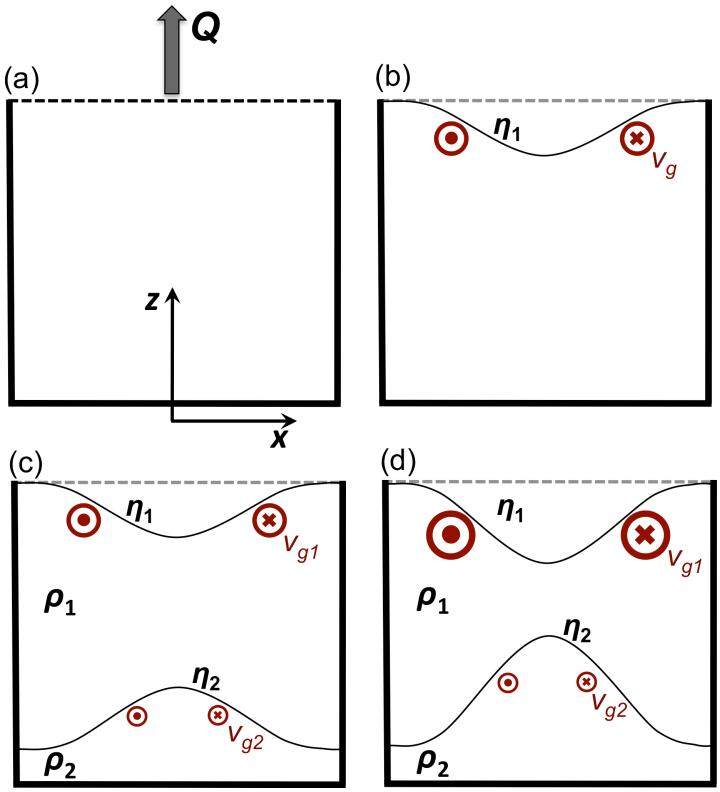

Figure 5.3: Conceptual two-dimensional illustration of the relationship between the surface elevation, sloping isopycnals and geostropic flow in a closed ocean basin on the northern hemisphere. Panel (a) shows a section trough the basin with an assumed transfer of heat (Q) from the ocean to the atmosphere. Panel (b) shows the resulting lowering of the ocean surface, denoted by $\eta_1(x)$, and the corresponding near-surface geostropic, cyclonic flow. Panel (c) shows a two-layer configuration consistent with reduced flow at depth, with layer 1 at top (with density ρ_1) and the more dense layer 2 ($\rho_2 > \rho_1$) below. The two layers are separated by the isopycnal interface $\eta_2(x)$. Panel (d) illustrates the relationship between a steepened internal isopycnal η_2, enhanced surface elevation and intensified geostropic flow, following Margules relation. x and z denote the upward and eastward directions, respectively.

5.5 Ocean response to different NAO composites

Figure 5.4 shows the SSH response to NAO^+ and NAO^-, as well the difference between the two composites, for the ERA40 and NCEP-NCAR composites. The largest amplitudes are found for the NAO^+ composite because of the strong atmospheric ocean forcing at NAO^+. The difference between the NAO^+ and NAO^- composites shows the same pattern as the SSH difference between the NAO^+ and NAO^n composites, see the upper left panels in Figs. 4.6 and 4.7, but with larger amplitudes. This demonstrates that the major signal in the NAO^+–NAO^- difference originates from the NAO^+ pattern, see lowermost panels in Fig. 5.4.

In section 4.3, comparisons between the ERA40 and NCEP-NCAR composites are given for the SLP, SSH, ocean temperature and salinity, and layer thickness. Despite that the two sets of composites are based on averages of different years, close agreement is found when the ocean conditions for a given NAO composite are compared for the two sets (see Fig. 4.5). However, the layer thickness showed some differences, specially for the NAO^- composite (see Fig. 4.12). The reason for the latter is likely because the analyzes were done in a relatively confined geographic region (transect through the LS), influenced by strong atmospheric forcing.

Differences between the two sets of composites tend to be larger when differences between NAO forcings are compared. This is specially noticeable for the difference between the NAO^- and NAO^n composites (right panels in Figs. 4.6 and 4.7) which show weak consistency. We also showed that the upper ocean heat content for NAO^+ forcing relative to a neutral state was larger for the ERA40 composites than the NCEP-NCAR composites (left, midle panels in Figs. 4.6 and 4.7). With the assumption of comparable ocean transport, the heat transport in the ERA40 composite exceeds that of the NCEP-NCAR composite. The same tendency is found for the difference between the NAO^+ and NAO^- composites, where an elevated SSH indicates warmer water, which is found along the NAC and STG (Fig. 5.4). Notice also that the amplitudes of the ERA40 composites in Fig. 5.2 are, in general, larger than the NCEP-NCAR composites. The latter seems to be the tendency throughout this study, which suggests larger differences between the strong and weak atmospheric forcing in the ERA40 composites. However, there is a degree of subjectivity in the degree of realisms derived from the NAO composites because

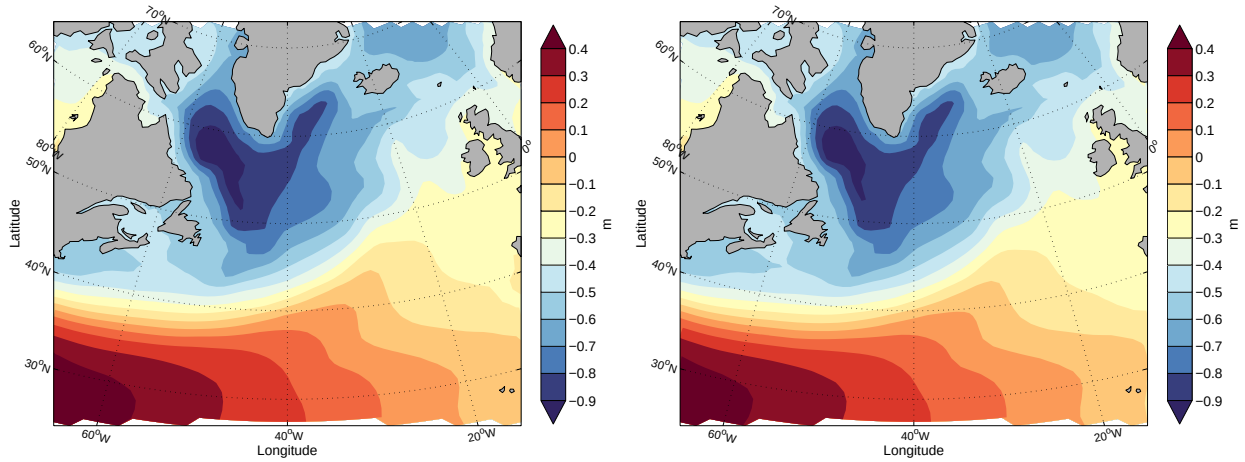

(a) NAO$^+$

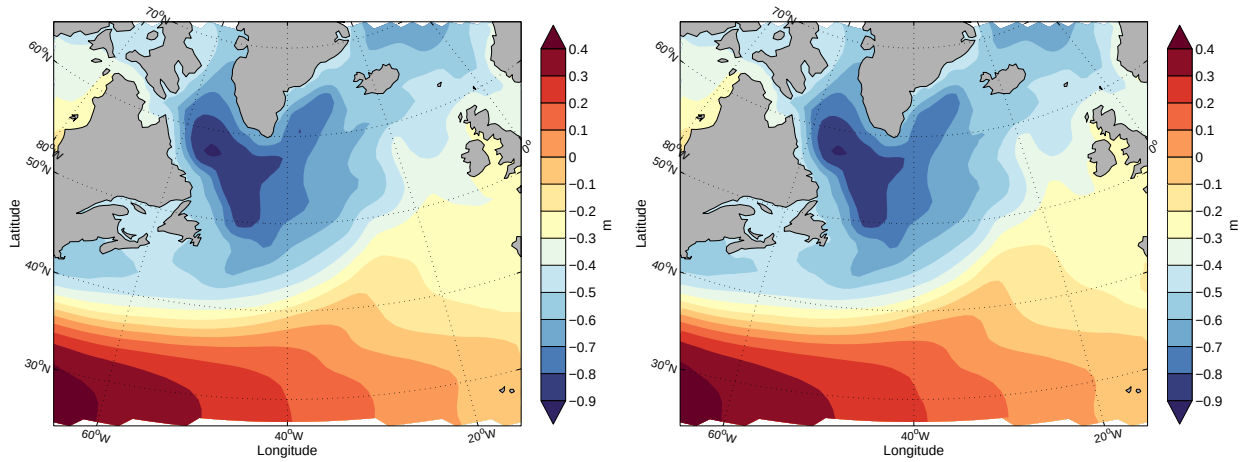

(b) NAO$^-$

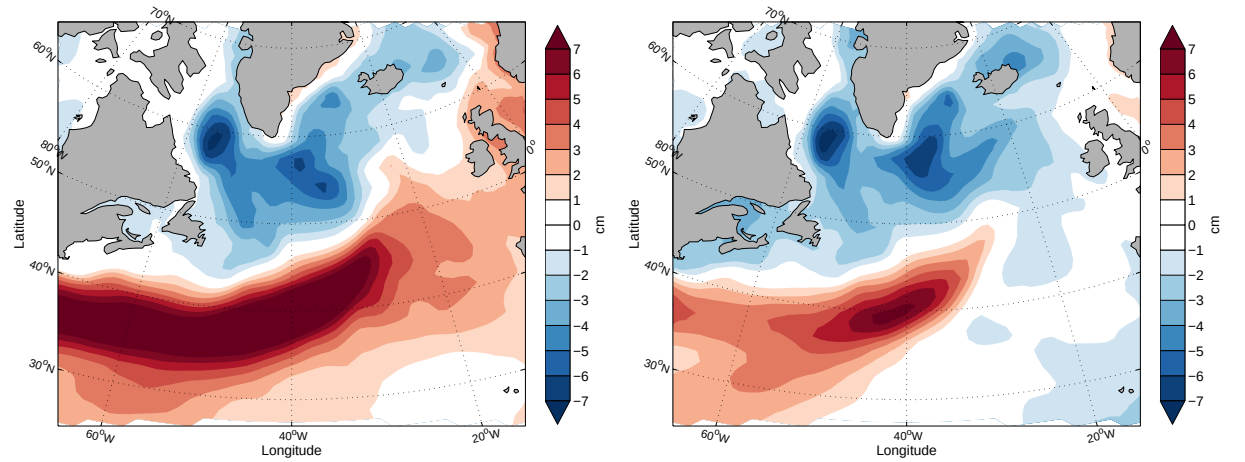

(c) NAO$^+$–NAO$^-$

Figure 5.4: SSH for NAO$^+$ composite in **(a)**, NAO$^-$ in **(b)**, and NAO$^+$ relative to NAO$^-$ in **(c)**. The left panels are based on the ERA40 NAO index, while the right panels are based on the NCEP-NCAR NAO index.

of lack of observations. Thus, we cannot conclude that any of the two NAO composites are more correct than the other.

The SSH and ocean temperature response to the NAO^+ forcing relative to the neutral state showed a dipolar pattern that follows the boundary between the SPG and STG, with a distinct signal along the NAC (see Figs. 4.6 and 4.7). The NAO^- forcing, however, does not resemble the oceanographic features in the area (like the dipolar pattern between the SPG and STG). As already mentioned, very weak consistency was found between the two sets of composites in the case of NAO^-. This suggests that the ocean response to the NAO^- forcing is much less consistent than the ocean response to the NAO^+ forcing, which makes it difficult to identify a typical pattern for the ocean's response to the NAO^- forcing.

5.6 Interpretation of EOF analyzes

The EOF patterns shown in section 4.5 represent the dominant mode of variability when seasonal variatons are not taken into account. The patterns can be interpreted as the main deviations from the mean state during the period 1960-2008, or 1993-2008 for the case with altimetry data. Similarities between the EOF analyzes strongly indicate a common physical cause behind the variability.

The EOF analysis of SSH is compared to the EOF analysis of altimetry data in Figs. 4.18 and 4.19. The altimetry and simulated EOF dipole patterns show an overall similarity for both the deseasonalized and winter average EOF's, but with differences in the location and distribution of the patterns. The major difference is a much stronger SSH drop east of 40 °W in the winter version of altimetry data compared to the SSH data. Despite different time intervals, the PC1 of the SSH is almost identical with the SPG index for the deseasonalized version. The correlations between the altimetry data and SPG index, however, is not significant different from zero at the 90% confidence level (see table 4.1). This puts some questions about whether the short-term variability in the simulated SPG index is realistic. The fact that the dominant mode of variability explain more of the variance in the data set for the SSH data than the altimetry data (54% and 36%, respectively), suggests that the simulated SSH is less complex and is unable to capture the

detailed dynamics and mechanisms that lead to the short-term variations in the data set. However, on a longer time scale the model simulates rather realistically the observed decrease in SSH between 1995 and 2008 (see Fig. 4.15(b)). This tendency suggests that the model is reasonably good at simulating inter-annual to decadal variations, which has also been demonstrated by previous studies (Hatun et al., 2005; Lohmann et al., 2008, 2009; Bentsen et al., 2013). It would also be interesting to analyze a longer data set of altimetry and compare this with the simulated SPG index. This would uncover whether the above results are typical or not. Unfortuneately, altimeter data was first available in 1993.

Figure 5.5 shows that the EOF patterns based on SSH, ocean temperature and salinity from 1960-2008 are in good agreement with the response from the NAO^+ and NAO^- forcings relative to a neutral state. Particular agreement is found for the NCEP-NCAR composites, which the EOF patterns are compared with. The ERA40 composites show also a close agreement, despite the ocean model is forced with reanalysis fields from the NCEP-NCAR based CORE2 reanalysis. The conclusion based on the NAO analysis strongly indicates that the variations in the SSH, ocean temperature and salinity EOFs are mainly determined by the atmospheric forcing, reflected by the NAO index.

The EOF pattern of the wind stress curl shows a negative anomaly located south of 60 °N and a positive anomaly close to Iceland, where negative curl values indicate an anticyclonic circulation anomaly (see Fig. 4.24). This pattern is in close agreement with Häkkinen and Rhines (2004, their Fig. 5). They also show EOF analysis of heat flux and corresponding PCs which are compared to the NAO index, where the wind stress curl is more related than the heat flux. The EOF analysis of the heat flux in this thesis shows a similar dipolar pattern as their EOF pattern, but a much stronger signal in the SPG which is consistent with strong heat loss from the ocean. This indicates a close relationship with the atmospheric forcing. We know that the NAO index reflects the storm activity in the North Atlantic, which through variations in the wind speed and air temperature, directly influences latent and sensible heat fluxes, as well the wind stress curl. Figure 5.6 confirms this where the leading PCs respond instantenous to the NAO forcing. In contrast to Häkkinen and Rhines (2004), heat flux is found to be more related to the NAO index than the wind stress curl, where the NAO index explains 50% and 28% of the variance of the corresponding PCs, respectively. The PC1 of the wind stress

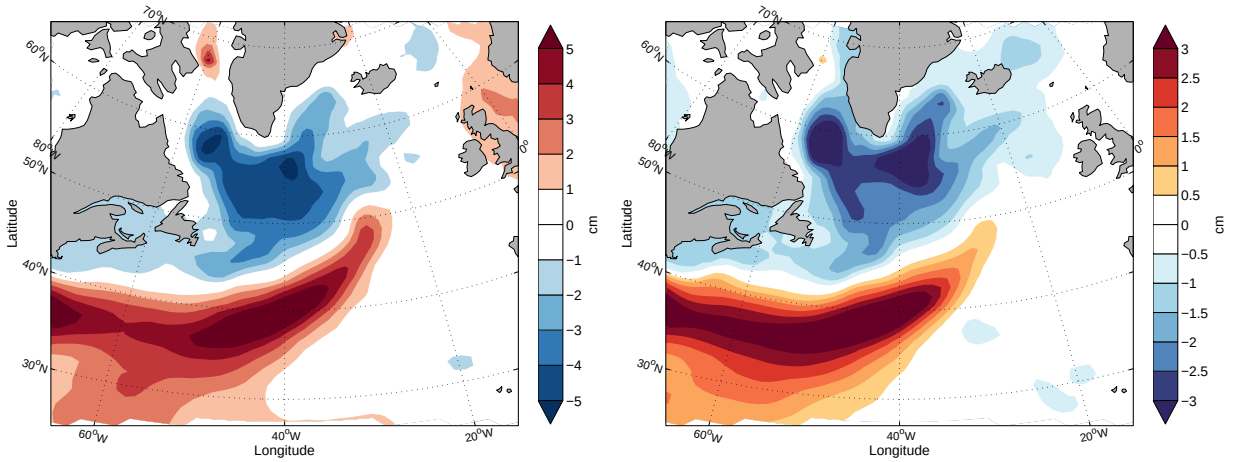

(a) SSH

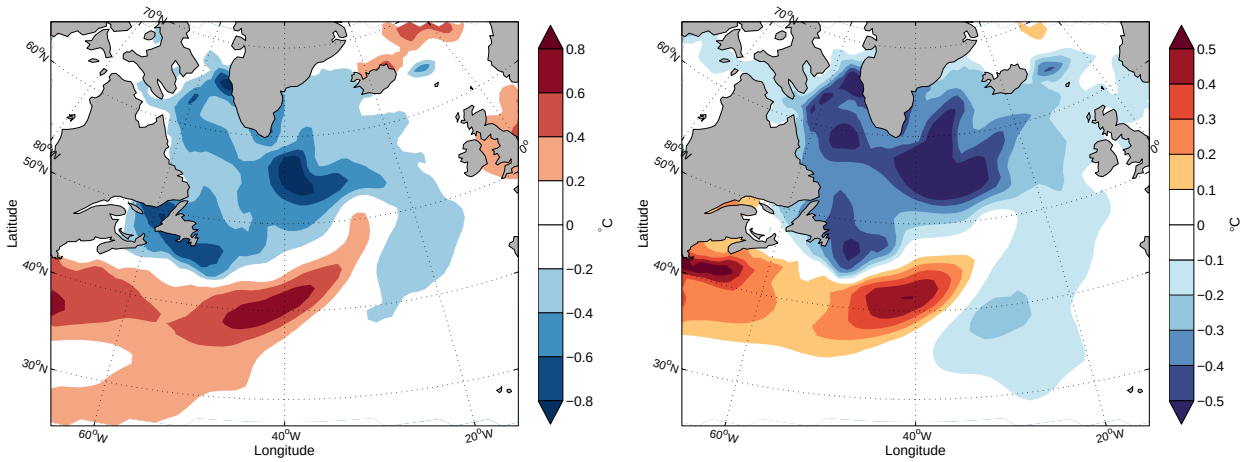

(b) OT

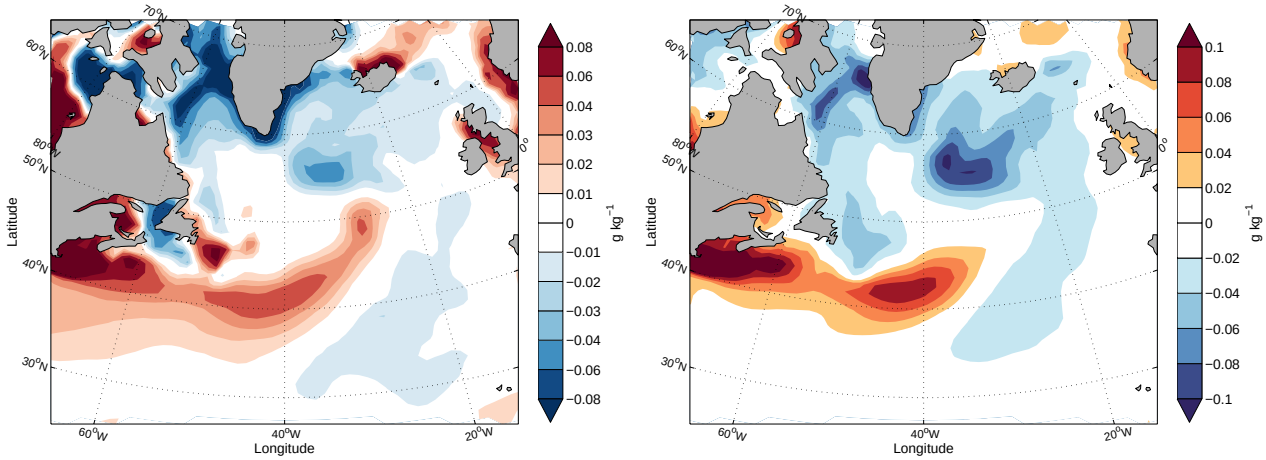

(c) OS

Figure 5.5: Left panels show the SSH, OT and OS response on the difference between years with NAO^{+} and NAO^{n} forcing from Fig. 4.7. Right panels show the corresponding response based on the EOF analyzes from section 4.5.

curl and heat flux also showed significant correlations at the 90% confidence interval with the SSH-based SPG index at 0 and 1 year lag, respectively (see table 4.2). The lag between the wind stress curl and heat flux seems to contradict the instantenous response of the wind stress curl to the NAO index. However, the correlation with SPG index was almost the same at 0 year lag, implying a robust response to the NAO-forcing.

The reason for showing the winter months based EOF patterns for the heat flux and wind stress curl is because the atmospheric forcing is strongest in winter. Since the NAO index embed variations in the heat flux and wind stress curl, these correlations are also strongest during winter. This is detected by the EOF analysis, where the variance explained by the winter averaged EOF analysis was larger and showed larger anomalies than the deseasonalized analysis (see table 4.2).

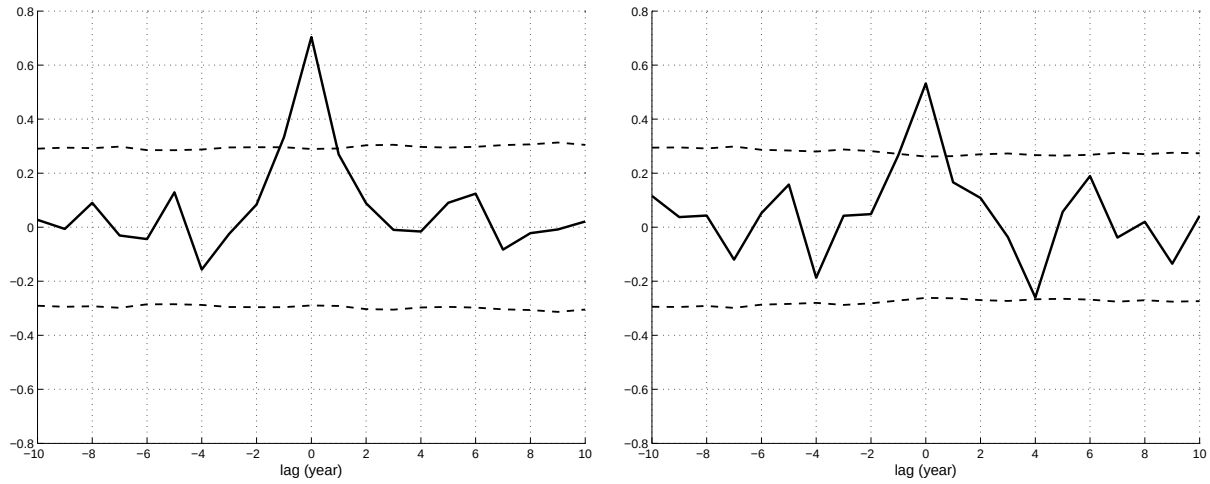

(a) Heat flux **(b)** Wind stress curl

Figure 5.6: Cross-correlation between the NAO index and the PC1 of the heat flux (left panel) and wind stress curl (right panel). Both PCs are based on the winter months. The dashed lines indicate the 95% confidence lines.

5.7 Cross-correlation between the AMOC and volume indices

The volume of layer 33 in the SPG, LS and IS has been analyzed and compared with indices of other variables Figs. 4.25 and 4.26. There is a tendency that the LS mixing take place prior to the convective mixing in the IS, with a lag of about 3-4 years. The

convective mixing during a winter of positive NAO index leads to an increase in the thickness of model layer 33. In the LS, this water occupy depths between 1000-2300 m and is a source to the southward component of the AMOC (Bentsen et al., 2004).

Based on an earlier version of the OGCM used in this thesis, Lohmann et al. (2008) found that the convective mixing associated with the thickness of the layers around 1500 m depth lead the strength of the AMOC by 7 years. They also found that the largest mixing anomalies during NAO^+ forcing occurs in the IS. However, they mention that the convective mixing in the IS might be overestimated due to the relative coarse horizontal resolution of their model. Bentsen et al. (2004) also used an earlier and more coarse resolution OGCM version than used here. In contrast to the result in this thesis, they found the convective mixing in the IS to take place a few years before the LS mixing. They also demonstrate that the convective mixing anomalies in the IS and LS may have opposite sign because the main driver of the convective mixing is different, where the NAO index leads the LS mixing and a local northward heat flux leads the IS. Thus, they conclude that the net effect from the SPG region that force the AMOC may be different from the effect from the LS alone.

The cross-correlations in this thesis support that the SPG volume is a combination of the LS and IS volume, with a peak correlation occuring between the peak correlation of the LS and IS. However, as seen in the cross-correlations, mixing in the IS responds to the AMOC instead of leading the AMOC, while the volume of layer 33 in the LS lead the AMOC by 0-2 years. This indicates that the IS is of less importance in the contribution to the AMOC than what is found in Bentsen et al. (2004) and Lohmann et al. (2008). This finding might be due to the higher horizontal resolution of the model used here. Considering that the LS showed the largest mixed layer depth and layer thickness of model layer 33, as well the fact that the volume in the LS leads the AMOC by 0-2 years, indicate that the convective mixing in the LS is a major source for the AMOC.

Chapter 6

Summary and Outlook

EOF analyzes and ocean response to atmospheric forcings represented by anomalously high, neutral and low NAO indices explain a large fraction of the variation in the North Atlantic marine climate. While EOF analyzes of heat flux and wind stress curl show instantaneous response to the NAO forcing, ocean temperature and salinity variations lag the NAO with one year. Variations in the SSH is found to be mainly determined by variations in near-surface ocean temperature. This is supported by the correlation between the SSH-based SPG index and PC1 of temperature and salinity, where temperature showed highest correlation. Variations in the ocean temperature and salinity are mainly found in the upper few hundred meters of the water column where the atmospheric forcing is directly felt.

Changes in the hydrography influences the buoyancy in the SPG, which may trigger convective mixing and subsequently the thickness of model layer 33. The volume of layer 33 shows inter-annual to decadal variations, with a more than doubling of the volume between a minimum in 1970 and a maximum in 1995. Much of this water is subsequently replaced by the volume from the above model layer 32. The major convective region in the model is found to be the LS, where the volume associated with the thickness of model layer 33 leads the AMOC at 41 °N by 0-2 years. No significant correlation at the 95% confidence level is found between the AMOC at 26.5 °N and any of the volume indices in the LS, SPG and IS, suggesting that the AMOC at this latitude is generally influenced by other mechanisms.

The SSH and barotropic streamfunction patterns show a coherent structure and co-variability in the SPG, with both working as indices of the SPG strength. The meaning of strength in this sense is how anomalously low the SSH gets, or how strong the barotropic streamfunction becomes. Variations in the SSH and barotropic streamfunction are both connected to variations in the atmospheric forcing, where the SSH leads the barotropic streamfunction by one year. Margules relation has been used to explain the governing mechanism driving the intensification of the circulation following an anomously strong domed density structure in the LS. The mechanism involves an increase in the geostrophic flow in the upper ocean which follows from the bell-shaped drop in SSH and steepened slope of the interface between model layer 32 and 33. We have demonstrated that the associated increase in the geostrophic flow in the upper ocean of about 5 Sv roughly explains the intensification of the barotropic streamfunction following NAO^+ forcing.

The EOF anayzes have shown that the heat flux is more related to the NAO index than the wind stress curl. However, both are important components in determining the marine climate in the North Atlantic. To understand what mechanism is most responsible for the changes in the SPG, sensitivity experiments with zero wind stress curl and zero heat fluxes could be run. This would give us an indication of what changes in the SPG strength is dominated by wind and the heat flux. Such experiments were planned as part of this thesis, but had to be cancelled because of limited time.

Whether an EOF-based or two-station based NAO index is used and what type of reanalysis it is based on, has shown noticeably effect on the ocean response to the difference between NAO composites. Thus, one should be careful in the choice of relying on one NAO index and a fixed definition of the NAO composites when analyzing the ocean response to the atmospheric forcing. This is specially the case on smaller spatial scales. A question that remains to be answered is whether there is a desirable choice between the two station based index or an EOF based index, and whether a model should use data from the same reanalysis as the model is forced with in the definition of the NAO index and corresponding NAO composites.

Another question that should be addressed is the usefulness of NAO as a proxy for the atmospheric forcing of the ocean, and whether this proxy is (essentially) constant

on longer time scales. Only very long reanalysis experiments (reanalysis experiments starting from the 1870's are currently being integrated) or analysis from multi-centennial coupled climate model simulations could address this central issue.

Appendix A

Statistical methods

Some statistical methods and definitions that are central in this thesis are described below. A more complete description can be found in Emery and Thomson (2004).

A.1 Mean

The mean of a vector x consisting of N data values is defined as

$$\overline{x} = \frac{1}{N} \sum_{i=1}^{N} x_i \tag{A.1}$$

A.2 Variance

The variance is a measure of the dispersion of the data values about the mean. The unbiased version is defined as

$$\sigma^2 = \frac{1}{N-1} \sum_{i=1}^{N} (x_i - \overline{x})^2, \tag{A.2}$$

where you need at least two values to define the variance.

A.3 Standard deviation

The standard deviation is the square root of the variance:

$$\sigma = \sqrt{\sigma^2} \tag{A.3}$$

A.4 Regression

Liner regression is a method of finding the linear relationship between a dependent and independent variable by fitting a straight line that best fits the scatterplot of the two variables. This line is defined as

$$y_i = b_0 + b_1 x_i + \epsilon_i, \tag{A.4}$$

where b_1 is the slope of the line, intercepting the y-axis at b_0. ϵ_i is the error of each data point i that are scattered along the regression line. After adopting the method of least squares, which minimizes the sum of the squared errors, b_1 and b_0 can be solved:

$$b_1 = \frac{\sum_{i=1}^{N}(x_i - \overline{x})(y_i - \overline{y})}{\sum_{i=1}^{N}(x_i - \overline{x})^2}, \qquad b_0 = \overline{y} - b_1\overline{x} \tag{A.5}$$

A.5 Correlation

The relationship between two variables can be determined by calculating the correlation coefficient

$$r = \frac{1}{N-1}\sum_{i=1}^{N}\frac{(x_i - \overline{x})(y_i - \overline{y})}{\sigma_x \sigma_y}, \tag{A.6}$$

where r ranges between -1 and 1. $r = 1$ mean that the vectors are identical, $r = -1$ mean that they are identical but inversely related, and $r = 0$ mean that there are no relationship between the values in the vectors.

A.6 t-test

Finding a high correlation between two data sets does not necessarily mean that the data sets are related, or share a common cause behind the variations (Emery and Thomson, 2004). The correlation may also have occured due to coincidence where the data sets happend to be similar by chance. The likelihood that the correlation did not occure by chance can be tested by doing a t-test. It involves defining a null hypothesis H_0, and an alternate hypothesis H_a. The definition of the alternative hypothesis determines if the t-test is one-sided or two-sided. Defining the alternative hypothesis as $r \neq 0$, and the null hypothesis as $r = 0$, means that the correlation is significant different from zero if the null hypothesis is rejected. The rejection of the null hypothesis involves the t-value

$$t = \frac{r\sqrt{n-2}}{\sqrt{1-r^2}}, \tag{A.7}$$

where n is the degree of freedom and r is the correlation. The null hypothesis is rejected if the calculated t-value is larger than the t-value found for the corresponding degrees of freedom and choice of significance level in the t-distribution curve, illustrated in Fig. A.1.

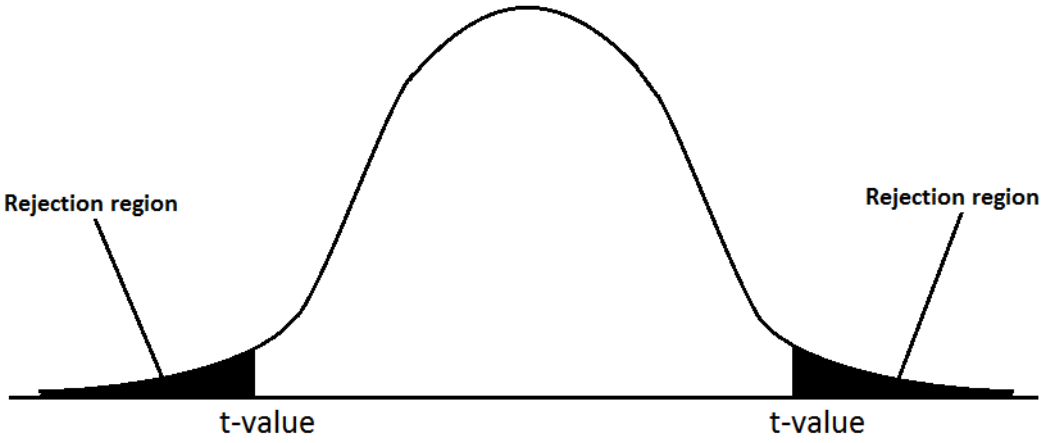

Figure A.1: Illustration of the t-distribution curve. The sharpness of the curve varies with the degrees of freedom. The black region is the area where the null hypothesis, H_0, can be rejected, which varies with the choice of significance level and associated t-value.

The null hypothesis can never be rejected by a 100% certainty because there is always a probability that two variables are identical by chance. However, if the significance level is low and corresponding rejection region small, the probability for an incorrect rejection of the null hypothesis is also small. For instance, a correlation above the significance

level of 0.1 means that there is a 10% chance that the rejection of the null hypothesis is incorrect or 90% likely that the calculated correlation did not occure by chance. This is analogous to saying that the correlation are significant above the 90 % confidence interval.

A.7 Empirical Orthogonal Functions analysis

In general, EOF analysis is a technique that generates a data set into modes of spatial variability that oscillates in time (Emery and Thomson, 2004). Each of these modes can be divided into a spatial pattern EOF that explains some of the spatial variations in the data set, and a time series known as PC containing temporal information about the corresponding EOF. Together they describe all of the variance in the data set, where the first mode explains the highest percentage of the total variance and the second mode the second highest percentage, and so on. Orthogonal functions mean that the functions (modes) are uncorrleated, where the integral of their product is zero. This mean that the variability in the modes are independent to one another.

In this thesis, a SVD is used to extract the leading EOFs and PCs in the data set, referred to as EOF1 and PC1, respectively. The SVD is a sophisticated, fast and relative simple method that involves decomposing the $M \times N$ data matrix D, into the product of three matrices: $D = USV^T$ (Emery and Thomson, 2004). U is an $M \times N$ orthogonal matrix whose elements are the eigenvectors, S is an $N \times N$ diagonal matrix containing the singular values of D down the diagonal, and V^T is the transpose of an $N \times N$ orthogonal matrix. Orthogonal means that each row in U, S and V are normal and independent to each other. The steps below is the procedure in which the EOFs and PCs are generated in this thesis.

1. A $M \times N$ matrix of a climate variable is defined, where each row contains information in the spatial domain and each column is the temporal variability of these spatial points.

2. The matrix is detrended by removing the mean value from each column containing the temporal information.

3. Each anomaly in the detrended matrix is weighted by the size of the corresponding grid cell. This is done because the grid size of the model are different (see Fig. 3.1).

4. The SVD method is used to find the U, S and V^T matrices, where the columns in V^T contains the PCs associated with each EOF. The EOFs are obtained from the product of U and S.

5. The amplitudes of the EOF pattern do not represent the real amplitude of the associated data set. In order to present the EOF1 pattern with realistic amplitudes, the normalized PC1 is regressed on the original data set.

6. The variance explained by each EOFs and corresponding PCs are obtained by using the square of the associated singular value from the diagonal matrix S divided by the square of the sum of all the singular values, which together explains 100% of the total variance in the data set.

Bibliography

Antonov, J. I., D. Seidov, T. P. Boyer, R. A. Locarnini, A. V Mishonov, H. E. Garcia, O. K. Baranova, M. M. Zweng and D. R. Johnson (2010). 'World Ocean Atlas 2009, Volume 2: Salinity'. *NOAA Atlas NESDIS* 69, p. 184.

Bentsen, M., I. Bethke, J. B. Debernard, T. Iversen, A. Kirkevåg, Ø. Seland, H. Drange, C. Roelandt, I. A. Seierstad, C. Hoose and J. E. Kristjánsson (2013). 'The Norwegian Earth System Model, NorESM1-M - Part 1: Description and basic evaluation of the physical climate'. *Geoscientific Model Development Discussions* 6, pp. 687–720.

Bentsen, M., H. Drange, T. Furevik and T. Zhou (2004). 'Simulated variability of the Atlantic meridional overturning circulation'. *Climate Dynamics* 22, pp. 701–720.

Bentsen, M., G. Evensen, H. Drange and A. D. Jenkins (1999). 'Coordinate transformation on a sphere using conformal mapping'. *Monthly Weather Review* 127, pp. 2733–2740.

Bleck, R., C. Rooth, D. Hu and L. Smith (1992). 'Salinity-driven thermocline transients in a wind- and thermohaline-forced isopycnic coordinate model of the North Atlantic'. *Journal of Physical Oceanography* 22, pp. 1486–1505.

Church, J.A., J.M. Gregory, N.J. White, S.M. Platten and J.X. Mitrovica (2011). 'Understanding and projecting sea level change'. *Oceanography* 24, pp. 130–143.

Collins, M., M. Botzet, A. Carril, H. Drange, A. Jouzeau, M. Latif, O. H. Otterå, H. Pohlmann, A. Sorteberg, R. Sutton and Terray L. (2006). 'Interannual to decadal climate predictability: A multi-perfect-model-ensemble study'. *Journal of Climate* 19, pp. 1195–1203.

Cunningham, S. A., T. Kanzow, D. Rayner, M. O. Baringer, W. E. Johns, J. Marotzke, H. R. Longworth, E. M. Grant, J. J.-M. Hirschi, L. M. Beal, C. S. Meinen and H. L. Bryden (2007). 'Temporal variability of the Atlantic meridional overturning circulation at 26.5 N'. *Science* 317, pp. 935–938.

Drinkwater, K. (2006). 'The regime shift of the 1920s and 1930s in the North Atlantic'. *ELSEVIER* 68, pp. 134–151.

— (2009). 'Comparison of the response of Atlantic cod (Gadus morhua) in the high-latitude regions of the North Atlantic during the warm periods of the 1920s-1960s and the 1990s-2000s'. *ELSEVIER* 56, pp. 2087–2096.

Eldevik, T, J. E.Ø. Nilsen, D. Iovino, K. A. Olsson, A. B. Sandø and H. Drange (2009). 'Observed sources and variability of Nordic seas overflow'. *Nature Geoscience* 2, pp. 406–410.

Emery, W. J. and R. E. Thomson (2004). *Data Analysis Methods in Physical Oceanography*. ELSEVIER Academic Press.

Furevik, Tore and J.E.Ø. Nilsen (2005). 'Large-scale atmospheric circulation variability and its impacts on the Nordic Seas Ocean climate-A review, in Drange et al. (eds)'. *The Nordic Seas: An integrated Perspective, Geophysical Monograph Series* 158, p. 105.

Griffies, S. M., B. L. Samuels and G. Danabasoglu (2012). *Coordinated Ocean-ice Reference Experiments - Phase II*. URL: http://www.clivar.org/wgomd/core/core-2#document.

Griffies, Stephen M., Claus Böning, Frank O. Bryan, Eric P. Chassignet, Rüdiger Gerdes, Hiroyasu Hasumi, Anthony Hirst, Anne-Marie Treguier and David Webb (2000). 'Developments in ocean climate modelling'. *ELSEVIER* 2, pp. 123–192.

Häkkinen, S. and P. B. Rhines (2004). 'Decline of subpolar North Atlantic circulation during the 1990s'. *Science* 304, pp. 555–559.

Häkkinen, Sirpa and Peter B Rhines (2009). 'Shifting surface currents in the northern North Atlantic Ocean'. *Geophysical Research* 114, p. C04005.

Hartmann, D.L (1994). *Global Physical Climatology*. Academic Press.

Hatun, H., M. R. Payne, G. Beaugrand, P. C. Reid, A. B. Sando, H. Drange, B. Hansen, J. A. Jacobsen and D. Bloch (2009). 'Large bio-geographical shifts in the north-eastern Atlantic Ocean: From the subpolar gyre, via plankton, to blue whiting and pilot whales'. *ELSEVIER* 80, pp. 149–162.

Hatun, H., A. B. Sando, H. Drange, B. Hansen and H. Valdimarsson (2005). 'Influence of the Atlantic subpolar gyre on the thermohaline circulation'. *Science* 309, pp. 1841–1844.

Hilmer, Michael and Thomas Jung (2000). 'Evidence for a recent change in the link between the North Atlantic Oscillation and Arctic sea ice export'. *Geophysical Research Letters* 27, pp. 989–992.

Holland, D. M., R. H. Thomas, B. De Young, M. H. Ribergaard and B. Lyberth (2008). 'Acceleration of Jakobshavn Isbrae triggered by warm subsurface ocean waters'. *Nature Geoscience* 1, pp. 659–664.

Hurrell, James W, Yochanan Kushnir, Geir Ottersen and Martin Visbeck (2003). 'An overview of the North Atlantic oscillation'. *Geophysical Monograph-American Geophysical Union* 134, pp. 1–36.

Hurrell, J.W. (1995). 'Decadal trends in the North Atlantic Oscillation: regional temperatures and precipitation'. *Science* 269, p. 676.

Iversen, T, M Bentsen, I Bethke, JB Debernard, A Kirkevåg, H Seland Øand Drange, JE Kristjansson, I Medhaug and M Sand (2013). 'The Norwegian Earth System Model, NorESM1-M-Part 2: Climate response and scenario projections'. *Geoscientific Model Development* 6, pp. 389–415.

Johns, WE, Molly O Baringer, LM Beal, SA Cunningham, Torsten Kanzow, Harry L Bryden, JJM Hirschi, J Marotzke, CS Meinen and B Shaw (2011). 'Continuous, array-based estimates of Atlantic Ocean heat transport at 26.5 N'. *Journal of Climate* 24, pp. 2429–2449.

Large, WG and SG Yeager (2009). 'The global climatology of an interannually varying air and sea flux data set'. *Climate Dynamics* 33, pp. 341–364.

Lazier, J., R. Hendry, A. Clarke, I. Yashayaev and P. Rhines (2002). 'Convection and restratification in the Labrador Sea, 1990-2000'. *Deep-sea Research Part I-oceanographic Research Papers* 49, pp. 1819–1835.

Locarnini, R. A., A. V. Mishonov, J. I. Antonov, T. P. Boyer, H. E. Garcia, O. K. Baranova, M. M. Zweng and D. R. Johnson (2010). 'World Ocean Atlas 2009, Volume 1: Temperature'. *NOAA Atlas NESDIS* 68, p. 184.

Lohmann, K., H. Drange and M. Bentsen (2008). 'Response of the North Atlantic subpolar gyre to persistent North Atlantic oscillation like forcing'. *Climate Dynamics* 32, pp. 273–285.

— (2009). 'A possible mechanism for the strong weakening of the North Atlantic subpolar gyre in the mid-1990s'. *Climate Dynamics* 36, p. L15602.

Lynn, R. J. (1971). 'On Potential Density in the Deep South Atlantic Ocean'. *Marine Research* 29, p. 7.

Marshall, J. and R.A. Plumb (2008). *Atmosphere, Ocean and Climate Dynamics: An Introductory Text*. ELSEVIER Academic Press.

Pickart, Robert S, Fiammetta Straneo and GW Kent Moore (2003). 'Is Labrador Sea Water formed in the Irminger basin?' *Deep Sea Research Part I: Oceanographic Research Papers* 50, pp. 23–52.

Press, W.H., S.A. Teukolsky, W.T. Vetterling and B.P. Flannery (1992). *Numerical Recipes*. Cambridge University Press.

Seager, R., D. S. Battisti, J. Yin, N. Gordon, N. Naik, A. C. Clement and M. A. Cane (2002). 'Is the Gulf Stream responsible for Europe's mild winters?' *Quarterly Journal of the Royal Meteorological Society* 128, pp. 2563–2586.

Stein, M (2005). 'North Atlantic subpolar gyre warming and impacts on Greenland offshore waters'. *Journal of Northwest Altantic Fishery Science* 36, pp. 43–54.

Stewart, R. H. (2008). *Introduction To Physical Oceanography*. Robert H. Stewart.

Talley, L., G. Pickard, W. Emery and J. Swift (2011). *Descriptive Physical Oceanography, Sixth Edition: An Introduction*. ELSEVIER Academic Press.

Thorpe, S.A (2007). *An Introduction to Ocean Turbulence*. Cambridge University Press.

Visbeck, M., E.P. Chassignet, R.G. Curry, T.L. Delworth, R.R. Dickson and G. Krahmann (2003). 'The ocean's response to North Atlantic Oscillation variability'. *Geophysical Monograph-American Geophysical Union* 134, pp. 113–146.

Yeager, S., A. Karspeck, G. Danabasoglu, J. Tribbia and H. Y. Teng (2012). 'A Decadal Prediction Case Study: Late Twentieth-Century North Atlantic Ocean Heat Content'. *Journal of Climate* 25, pp. 5173–5189.